Ocean Engineering 245 (2022) 110397

Contents lists available at ScienceDirect

Ocean Engineering

journal homepage: www.elsevier.com/locate/oceaneng

Comparative investigation: Closed versus semi-closed vertical cylinder-shaped fish cage in waves

Yugao Shen [a,b,*], Reza Firoozkoohi [a,d], Marilena Greco [a,b,c], Odd M. Faltinsen [a,b]

[a] Department of Marine Technology, Norwegian University of Science and Technology (NTNU), Trondheim, NO-7491, Norway
[b] Centre for Autonomous Marine Operations and Systems, NTNU AMOS, Trondheim, NO-7491, Norway
[c] CNR-INM, Institute of Marine Engineering, Rome, Italy
[d] Sintef Ocean, Trondheim, Norway

ARTICLE INFO

Keywords:
Closed and semi-closed cages
Regular and irregular waves
Global response
Interior waves
Mean drift forces
Survival conditions

ABSTRACT

A comparative analysis between a closed cage (CC) and a semi-closed/open-bottom cage (OC) in regular, white-noise and irregular waves is presented. Both cages consist of a vertical circular free surface-piercing cylinder with an external toroidal floater. A main target is to examine experimentally and theoretically the similarities and differences of the hydrodynamic behavior between the two cages. Transfer functions obtained from regular and white-noise waves test show that the two cages have similar performance in surge motion, ovalizing deformations, interior wave elevation and mean drift loads in shorter waves (wavelength to cage diameter ratio $\lambda/D < 1$). This is not the case for heave, with OC experiencing much larger heave. A clear sinkage (minus average heave) is also observed for OC, which is almost proportional to the square of the incident wave amplitude. The linear potential flow solver WAMIT can provide a reasonable prediction of surge and pitch motions, and mean drift loads for OC in shorter waves ($\lambda/D < 1.5$), but is unsatisfactory in longer waves and, in general, for heave motion.

From the analysis of irregular wave tests, there is a small difference in the standard deviations of the surge motion (wave-frequency component) and interior waves for the semi-closed and closed cages. The slow-drift component is dominant in surge for both cages, with OC having a smaller value due to larger viscous damping associated with flow separation at the bottom. Theoretical evaluations of standard deviations based on transfer functions from a white-noise test and from WAMIT are performed, assuming that the linear superposition principle applies. Reasonable agreement against results from experiments in irregular waves is achieved except for response variables with strong nonlinear effects.

Survival conditions for both cages are determined through systematic evaluations. The platform freeboard is identified as the most critical parameter. The minimum freeboard for the closed and semi-closed cage should be at least 1.05 and 1.3 m, respectively, to operate at moderate exposure sea states. The standard deviation of vertical acceleration due to rigid body motions and interior waves could reach 0.72 m/s^2 for both cages at high exposure sea states, which might be of concern for fish inside.

1. Introduction

Salmon lice becomes an important challenge for the Norwegian aquaculture industry nowadays. Stricter regulations have been imposed by the Norwegian government to limit the spread of salmon lice larvae from farmed to wild salmon. The treatment of sea lice could constitute more than 10% of production costs (Iversen et al., 2015) and the high cost of delousing treatments has led to the development of preventive sea cage designs, such as skirt sea cages (Grøntvedt and Kristoffersen, 2015), semi-closed and closed floating containment cages (Nilsen et al., 2017). Based on the fact that the salmon lice larvae are with a higher density in the upper layer of the water column (Geitung et al., 2019; Huse and Holm, 1993; Jones and Beamish, 2011; Oppedal et al., 2017) and that salmon develops higher infestation when staying near the sea surface than at larger submergence (Hevrøy et al., 2003), it is expected that putting a tarpaulin around the upper few meters of a traditional cage (a skirt) will reduce lice infestation rates on the farmed salmon. Skirt sea cages (e.g. see Fig. 1(a)) have been widely used in the industry and proved to be an effective approach to reduce the sea lice (Grøntvedt and Kristoffersen, 2015; Lien et al., 2016). The main drawback is that the shielding skirt is typically made of tarpaulin, thus it can have large

* Corresponding author at: Department of Marine Technology, Norwegian University of Science and Technology (NTNU), Trondheim, NO-7491, Norway.
E-mail address: yugao.shen@ntnu.no (Y. Shen).

https://doi.org/10.1016/j.oceaneng.2021.110397
Received 6 July 2021; Received in revised form 6 November 2021; Accepted 12 December 2021
Available online 10 January 2022

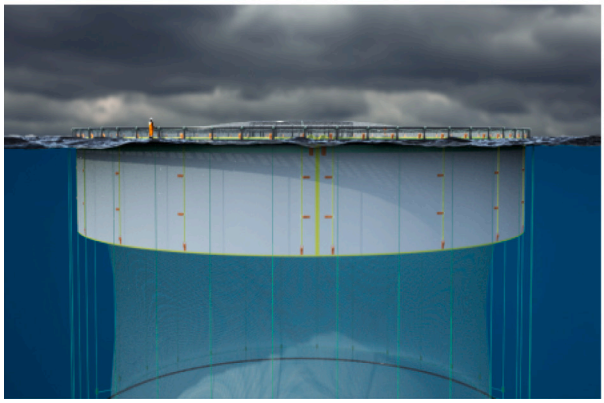

(a) Tarpaulin lice skirt around a traditional net cage (FiiZK, 2021).

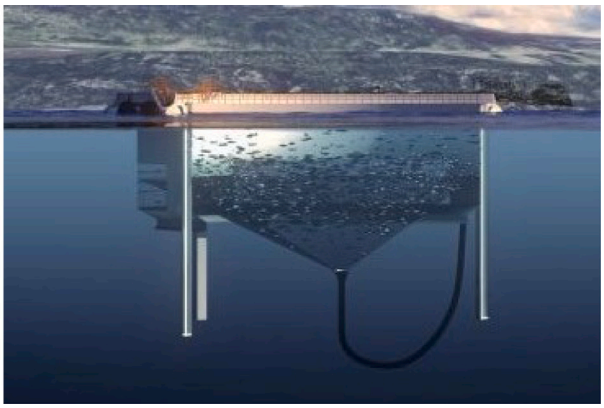

(b) Steel skirt for a semi-closed cage (Aquatraz, 2021).

Fig. 1. Sketches of a traditional net cage with flexible sea skirt (a) and a novel semi-closed cage with netting attached to the bottom (b) (FiiZK, 2021; Aquatraz, 2021).

deformations in strong currents, resulting in potentially less obstruction for the current and lice (Lien et al., 2014). Closed cage concepts were introduced to have a full control of the interior water quality (Nilsen et al., 2017; Strand et al., 2016). The physical contact between the infective sea lice larvae and the salmon host could be prevented by pumping and filtering water from sufficiently large depth into enclosed cages. An alternative semi-closed fish cage concept was developed, equipped with deep steel side wall, also referred to as steel skirt, with a traditional net cage attached to the bottom (see Fig. 1(b)) to prevent fish escape. A water circulation system is needed to pull in oxygen-rich water from submergence free from sea lice and algae, and to force it to move in the cage. This cage concept could be seen as a hybrid between a closed cage and a skirt cage.

For all the mentioned novel cage concepts, few existing studies are available. To guarantee structural safety and fish welfare, a better understanding of the behavior of the different cage concepts is necessary. For a traditional net cage with skirt, the skirt is highly flexible. The estimation of its response in waves and current could be quite challenging and is beyond the scope of the present study. For the closed cage, we carried out an experimental and theoretical study on wave-induced response of a closed floating fish cage (Shen et al., 2021). It consists of a vertical circular cylinder with an external toroidal floater. The influence of sloshing of the water inside the cage on the global response of the cage, the interior wave elevation and the mean drift loads, was examined. The analysis highlighted that the cage did not behave as fully rigid. Actually, ovalizing radial deformations were found to be rather important in affecting the features of the waves inside the cage. The behavior of semi-closed cage in waves was examined only in few available studies and represents the focus of the present paper. Important aspects to be examined relate to operational behavior and survivability of the system. For the survivability, (1) the mooring-line integrity and (2) the fish welfare represent two relevant criteria. The horizontal motions represent an example of critical response variable for (1), while the vertical acceleration of the interior water is an example of critical response variable for (2). In this context, a driving question of our research is: will the semi-closed cage has similar hydrodynamic behavior in waves as a closed cage with the same dimensions? To answer this question, we investigated the dynamic response of a semi-closed/open bottom cage in waves through model tests and numerical calculations. To facilitate the comparison, the chosen open-bottom model resembles the overall geometry and stiffness of the closed cage model in Shen et al. (2021). One should note that, an operating semi-closed cage will have a netting attached to the cage bottom (as shown in Fig. 1(b)). The bottom net was not considered in the present experiments to reduce complexity. On the other hand, it is expected to have a small contribution to the global response of the system and its effect can be simplified as an additional small damping effect. Detailed assessment of the bottom cage influence is not discussed here and is left as a future work.

To find relevant studies for the semi-closed cage system, a thorough literature review has been performed. For the exterior floating collar, many investigations have been conducted, for instance by Li and Faltinsen (2012) to investigate the wave-induced vertical response of an elastic circular collar in waves and by Park et al. (2020) to improve the estimation of drag coefficients of floating collars. There is not much available literature directly connected with semi-closed cages but the water flow through the bottom of such cages has some similarities with e.g. the water flow through moonpools. Many investigations have been performed on the dynamic response of a ship with a moonpool, for instance those by Molin (2001), Kristiansen and Faltinsen (2008), Newman (2018), Ravinthrakumar et al. (2020), Xu et al. (2020) and could be enlightening for the present study. Nevertheless, we should note that there exist some important differences between a ship with a moonpool and a semi-closed cage. First of all, a semi-closed cage has a relatively thin wall thickness, which means that the ratio between the characteristic dimension of the inner open part of the cage (i.e. interior diameter) and that of the whole cage (i.e. outer diameter) is close to 1, while for a ship the ratio in beam direction is typically less than 1/2. The relative large ratio between the inner diameter and outer diameter of a cage can significantly reduce the metacentric height in roll/pitch and thus change the seakeeping behavior of the system, compared with a traditional ship. In addition, piston mode resonance inside the moonpool is of primary concern for a ship. Piston resonance refers to the lowest resonant mode of the water motion in a semi-entrained volume of fluid with a free surface (see e.g. Kristiansen and Faltinsen (2008)). An important feature is that the space-averaged vertical water velocity is non-zero. For a semi-closed cage, apart from possible piston resonance, wave-induced sloshing could also become an issue, similarly as for a closed cage. Hydro-elasticity may also matter due to the fact that the cage is with a thin side wall, compared with a ship.

The present paper is structured as follows. In Section 2, a brief description of the experimental set up for the semi-closed cage is given. Relevant information for the closed cage in Shen et al. (2021) is also provided for clarification purpose. Experimental results for the semi-closed cage in regular waves and white-noise waves are then given and analyzed in Section 3. The focus is on the transfer functions of rigid body motions, radial elastic deformations, internal sloshing and mean wave drift forces in the range of wave periods associated with local wind generated waves. Numerical results from the linear potential flow solver WAMIT, assuming a rigid body, are also provided to assess the possibility of employing linear potential flow theory to describe the system. The motivation to do this is that in engineering practice this

Table 1
Norwegian aquaculture site classification for waves and current (StandardNorge, 2009). H_s: significant wave height; T_p: peak period; U_∞: current velocity. It is assumed irregular waves for each wave class. If regular wave is considered, the standard says that the corresponding wave height H can be assumed to be 1.9 times the significant wave height.

Wave	H_s(m)	T_p(s)	Exposure	Current	U_∞(m/s)	Exposure
A	0.0–0.5	0.0–2.0	Small	a	0.0–0.3	Small
B	0.5–1.0	1.6–3.2	Moderate	b	0.3–0.5	Moderate
C	1.0–2.0	2.5–5.1	Heavy	c	0.5–1.0	Heavy
D	2.0–3.0	4.0–6.7	High	d	1.0–1.5	High
E	>3.0	5.3–18.0	Extreme	e	>1.5	Extreme

Table 2
Scaling factors.

Parameter	Scaling factor	Value	Unit
Length	λ	27	m
Velocity	$\lambda^{1/2}$	5.19	m/s
Acceleration	λ^0	1	m/s^2
Angle	λ^0	1	deg
Force	$1.025\lambda^3$	2.107×10^4	N
Moment	$1.025\lambda^4$	5.447×10^5	Nm
Mass	$1.025\lambda^3$	2.107×10^4	kg
Time	$\lambda^{1/2}$	5.19	s

type of tools is normally used at design phase; it is, therefore, important to assess their capability and accuracy to predict the response of such novel fish-farm concepts. Comparisons of transfer functions between the semi-closed and closed cages are also presented. To represent more realistic sea conditions, model tests for both cages in irregular waves were also performed and corresponding results are discussed in Section 4. The standard deviations of relevant response variables were estimated and used as basis for determining the survival conditions for the two cages in Section 5. To do this, systematic calculations were carried out examining sea states from small exposure to high exposure conditions, according to the Norwegian aquaculture site classification, see Table 1.

2. Experimental setup

Model tests were performed in the Ocean Basin Laboratory at the Marine Technology Center in Trondheim. The basin has an overall length of 80 m and width of 50 m. The depth can vary between 0–10 m by means of an adjustable bottom and was set to 5 m.

A detailed description of the experimental set-up has been given in Shen et al. (2021) in connection with the experiments in waves of the closed-cage model. In this part, we focus on the experimental set-up of the semi-closed cage model. A brief description of the closed-cage model is also provided for illustrating the similarities and differences between the two cage models.

The physical open cage model used in the experiments consisted of a vertical bottomless cylindrical cage, as shown in Fig. 2(a). A model test scale ratio of λ =1:27 was in mind and Froude scaling with geometric similarity was assumed. Correct representation of gravitational and inertial forces were thereby ensured through using the scaling factors presented in Table 2, where the factor 1.025 reflects the ratio between density of salt and fresh water. Two Cartesian right-handed coordinate systems were implemented in the model tests, one global system $Oxyz$ related to the basin and one local system fixed to the model. The origin of the former is in the plane of undisturbed free surface with vertical z-axis positive upwards through the center of the cage in calm water and positive x towards the wavemaker, see Fig. 4.

2.1. Cage model description

Photo of the semi-closed cage model from the front camera is presented in Fig. 2(a). A sketch of the model and detailed dimensions are illustrated in Fig. 3(a). The open bottom model was manufactured to resemble the overall geometry and stiffness of the original closed cage model (shown in Fig. 2(b) and Fig. 3(b)) studied in Shen et al. (2021). Similar floating collar and vertical aluminum plates were installed. To compensate for the reduced displaced mass of the internal volume, the model was equipped with a band of buoyancy elements manufactured from Divynicell blocks, which were mounted around the bottom. Detailed descriptions are given below.

The semi-closed model consisted of a vertical circular cylinder with draft h =0.75 m and outer diameter $D = 2R$ = 1.5 m. The side wall of the cylindrical cage was made of polycarbonate resin (Lexan) with thickness t_c= 5 mm. The resulting internal diameter is $D_t = 2R_t$ = 1.49 m. A semi-submerged torus shaped floating collar was attached to the outside part of the cylindrical cage. The floating collar was made of plastic electrical tube with cross-sectional diameter d_f = 0.05 m. Three groups of vertical aluminum plates (both inside and outside the tank) were used to connect the polycarbonate plate. They are evenly distributed with a separation angle of 120 degree. The position of one of the plates relative to the incident wave is θ = 95.54°, indicating a slight asymmetry of the model with respect to the $x-z$ plane (see Fig. 4). A band of buoyancy elements was installed around the bottom to provide additional buoyancy. The band was made of Divynicell with a thickness of 0.02 m and a height of 0.25 m, as illustrated in Fig. 3(a). The freeboard of the model was h_u=0.35 m to prevent spilling of water in case of large wave-induced pitch/roll motions. The main particulars of the semi-closed and closed cage models are given in Table 3. The center of buoyancy and metacentric height for the closed cage given here are different from those shown in Shen et al. (2021). The reason is that the values given in Shen et al. (2021) are defined for combined cage wall and internal fluid, while here are just for the cage solid wall, to be consistent with the open-cage definitions. For the semi-closed cage model, the cylindrical part (including bottom buoyancy elements) contributes to about 90% of the total buoyancy of the cage while the floating collar contributes to about 90% of the restoring stiffness for heave and about 100% for pitch when at rest and half submerged. A consequence is that the heave and pitch response can be quite sensitive to the change of the weight and can be quite nonlinear due to the fact that the floating collar possesses highly curved cross-sectional profile near the mean waterline.

2.2. Instrumentation

The same instruments used for the closed cage were employed, as shown in Fig. 2. An optical positioning system (Qualisys Oqus) was applied to track the position of markers mounted on the model. Eight markers (Pos1-8 in Fig. 4) were installed along the perimeter of the cage model at freeboard level, i.e., h_u=0.35 m, such that also flexible radial deformations of the cage could be detected. A set of three markers was also installed for 6 degree-of-freedom rigid-body motions tracking (see the white box installed at the freeboard of the cage in Fig. 2(a)). Wave induced accelerations of the model were measured by three accelerometers (placed at the angular positions θ = 345.5°, 225.2° and 105.2°) mounted on the cage side wall at a height of 0.1 m above the mean free surface. Pairs of internal (RW1-8) and external (RW9-16) conventional wave probes were installed and distributed radially at eight positions along the side wall with a radial distance $0.05R$ from the cage wall. The local wave elevation was measured in the body-fixed reference frame, so it is influenced, in principle, by both rigid body motions and possible interior sloshing. Detailed arrangement of the markers, accelerometers and wave probes is illustrated in Fig. 4.

2.3. Mooring system description

Both cage models were moored with four mooring lines in the horizontal plane, evenly distributed with 90° between each, see Fig. 4. Each of the four mooring lines was attached far away directly to

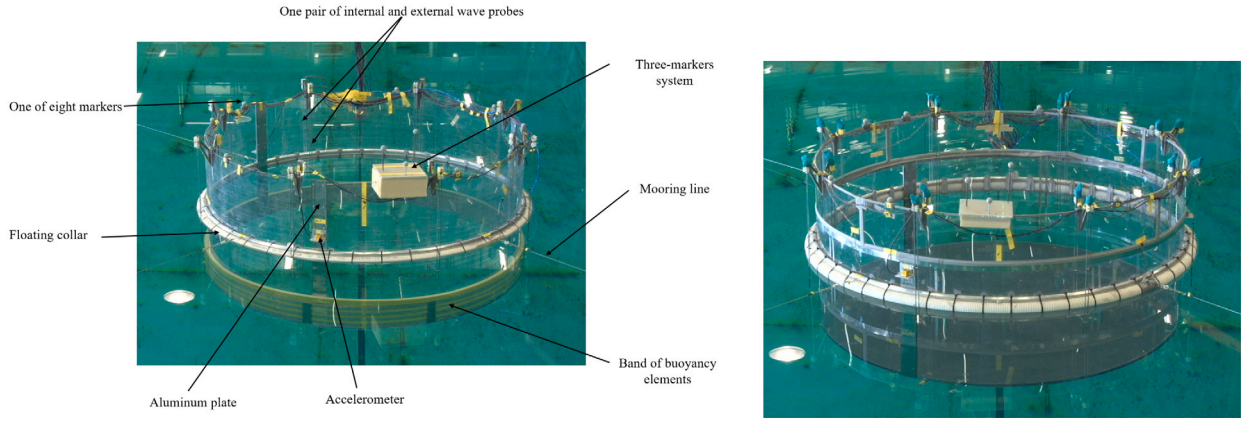

(a) Open-bottom cage (b) Closed cage

Fig. 2. Front-camera photo of the physical model for the open-bottom cage (a) and closed cage (b), respectively.

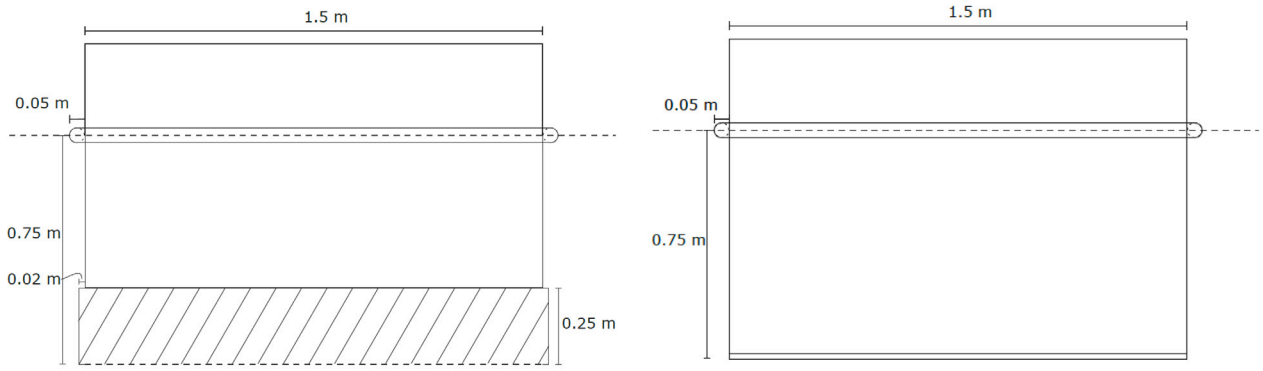

(a) Open-bottom cage (b) Closed cage

Fig. 3. Sketch and dimensions of the physical model for the open-bottom cage (a) and closed cage (b), respectively.

Table 3
Parameters of the cage models. Both model-scale and full-scale values are provided.

Parameter	Symbol	Open cage		Closed cage		Unit
		Model scale	Full scale	Model scale	Full scale	
Diameter	D	1.5	40.5	1.5	40.5	m
Draft	h	0.75	20.25	0.75	20.25	m
Freeboard	h_u	0.35	9.45	0.35	9.45	m
Mass	M	49.2	9.924×10^5	69.0	1.392×10^6	kg
Center of gravity (COG)	z_g	−0.199	−5.373	−0.360	−9.72	m
Center of buoyancy (COB)	z_b	−0.451	−12.177	−0.553	−14.931	m
Moment of inertia x-axis	I_{xx}	19.5	2.868×10^8	25.86	3.8×10^8	kg m^2
Moment of inertia y-axis	I_{yy}	19.5	2.868×10^8	25.86	3.8×10^8	kg m^2
Moment of inertia z-axis	I_{zz}	28.0	4.12×10^8	31.98	4.7×10^8	kg m^2
Metacentric height	GM	1.367	36.909	3.0	81	m

horizontal free-hanging coil springs. The ends of the front two mooring lines (L1 and L4 in Fig. 4) were placed 1 m above the calm water surface while the aft two lines (L2 and L3 in Fig. 4) were placed to 0.6 m to avoid contact with water and disturbance of waves during the tests. The stiffness of each coil spring was 60 N/m, yielding an equivalent stiffness k_s = 169.7 N/m (132.4 kN/m full-scale) in x and in y directions for the system. Tension in each mooring line was measured by an uni-axial load-cell that connected the mooring line to the cage. Since the mooring lines considered are quite long, approximately 33 m each, the small height difference in the far away ends will cause a negligible staticpitch. The used set-up ensured practically linear mooring-line stiffness effects, as confirmed by the surge free-decay tests, and a small influence of the mooring-lines on the vertical platform motions.

2.4. Test conditions

Both cage models were tested in regular waves and truncated white-noise waves. The term truncated white noise is used to describe a band limited white noise spectrum, i.e. a square spectrum with nearly equal energy for all frequencies within the upper and lower bounds, and with zero energy outside the bounds. Hereafter the truncated white-noise tests will be indicated as white-noise tests. All tests were performed twice to check the repeatability of the measurements. Good repeatability was observed. This fact and the consistence among regular and white-noise wave tests when linear effects are dominant (see Section 3) support a satisfactory reliability of the experimental results. The regular wave tests were performed at a fixed wave steepness H/λ

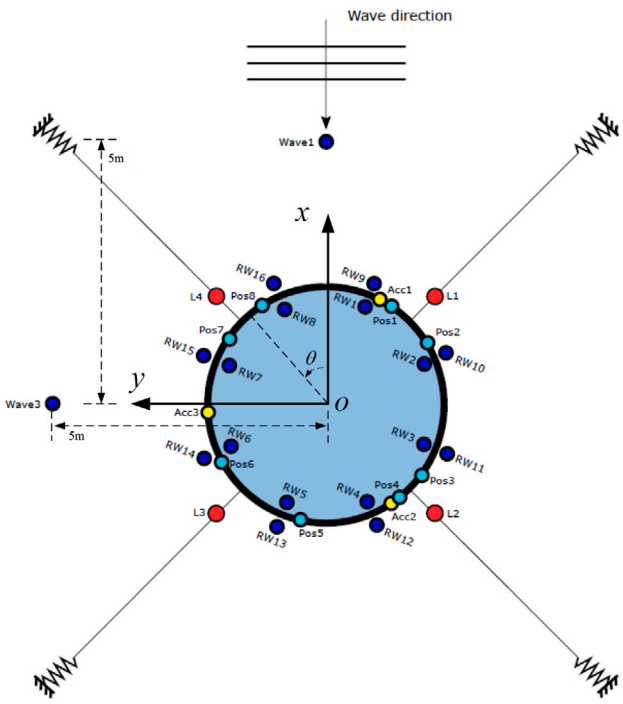

Fig. 4. Sketch of the instrumentation setup from top view. Blue circles: interior and exterior wave probes. Sky-blue circles: optical positioning markers. Yellow circles: accelerometers. Red circles: force transducers. Definition of Cartesian Earth-fixed coordinate system $Oxyz$ is also given with origin in mean free surface and positive z upwards.

Table 4
Test matrix for open-bottom cage (OC) showing prototype (full-scale) significant wave height H_s and peak wave period T_p and spectral peakedness γ. For the white-noise tests, the lower and upper incident-period region were 3 s and 20 s.

Name	Spectrum	T_p(s)	H_s(m)	γ
WH-1	White noise	–	1.0	–
WH-2	White noise	–	2.0	–
IRR-1	JONSWAP	5	1.5	2.87
IRR-2	JONSWAP	6	2.0	2.39

$= 1/60$, with H as the wave height and λ as the wave length. In total 23 wave periods were considered varying from 0.6 s to 1.55 s. The corresponding wavelength-to-diameter ratio λ/D changes from 0.38 to 2.5. Some additional tests were performed at higher wave steepness $H/\lambda = 1/45$. The duration of each regular-wave test was about 2.3 min. Two series of white-noise tests were performed to obtain continuous transfer functions within a given frequency region. The examined lower and upper period region were 0.577 s (3 s full-scale) and 3.85 s (20 s full-scale) and two significant wave heights were considered with H_s = 0.037 m (1 m full-scale) and 0.074 m (2 m full-scale), respectively.

Two irregular wave tests were also performed for both the closed and semi-closed cages to represent more realistic sea states. The irregular waves were generated according to the definition of JONSWAP wave spectrum. The test matrix of the white-noise waves and irregular waves is shown in Table 4. The duration of each white-noise and irregular-wave test was 34.6 min (3 h full-scale).

2.5. Signal processing

Detailed explanations concerning the approach to extract rigid body motions and radial elastic deformations from the measured translatory displacements of eight markers installed at the freeboard of the cage, and the procedure to identify the sloshing modes from the interior eight wave probes (RW1-8), as well as the strategies to obtain steady-state responses in regular waves and transfer functions from the white-noise/irregular-wave tests, are documented in Shen et al. (2021), so they are omitted here.

2.6. Decay tests

Free decay tests for the semi-closed cage were carried out in surge, heave and pitch in calm water to estimate the uncoupled natural periods and resonant damping ratios of these motions in ambient calm water. Here uncoupled denotes that coupling between surge, heave and pitch is neglected. As an example, time history of the surge motion during a free decay is shown in Fig. 5(a). The obtained natural period in surge is $T_{n,1,o} = 19.56$ s (101.6 s full-scale). The surge motion η_1 of a cage during a free decay test is assumed to be described by the following one degree of freedom (DOF) equation

$$\left[M + A_{11}(0)\right]\ddot{\eta}_1 + B_{11}^{lin}\dot{\eta}_1 + B_D\dot{\eta}_1\left|\dot{\eta}_1\right| + k_s\eta_1 = 0 \tag{1}$$

where $\ddot{\eta}_1 = d^2\eta_1/dt^2$ and $\dot{\eta}_1 = d\eta_1/dt$ are the acceleration and velocity in surge, M is the mass of the cage and $A_{11}(0)$ is the zero frequency added mass in surge, as an approximation of the added mass at the surge natural period. k_s is the equivalent stiffness of the cage in surge. B_{11}^{lin} is linear damping while B_D is associated with eddy-making quadratic damping. The latter can be further expressed as $B_D = 0.5\rho h D C_D$, with ρ the water density, h the draft of the cage and C_D the drag coefficient of the cage. Assuming a constant C_D and following the procedure by Faltinsen (1993), a linear damping coefficient $p_1 = B_{11}^{lin}/[M + A_{11}(0)]$ and a quadratic damping coefficient $p_2 = B_D/[M + A_{11}(0)]$ can readily be obtained, see Fig. 5(b). The corresponding drag coefficient is $C_D = 14.1$. From the results, the quadratic damping is dominant, which is intuitively reasonable, as flow can easily separate with important vortex shedding at the open bottom with sharp corner.

The natural periods for heave and pitch derived from the free-decay tests are $T_{n,3,o} = 1.13$ s (5.87 s full-scale) and $T_{n,5,o} = 1.98$ s (10.3 s full-scale), respectively. The associated damping coefficients p_1 and p_2 are difficult to estimate due to scattered oscillation amplitudes.

Free decay tests in surge and pitch for the closed cage were also performed (Shen et al., 2021). The corresponding natural periods are $T_{n,1,c} = 22.4$ s (116.4 s full-scale) and $T_{n,5,c} = 2.76$ s (14.36 s full-scale), respectively. There are no experimental data concerning heave free-decay response. The heave natural period $T_{n,3,c}$ is instead obtained from a white-noise test, corresponding to the peak period of the evaluated heave transfer function, with $T_{n,3,c} = 2.12$ s (11 s full-scale). A constant drag coefficient C_D for surge motion is assumed and found to be well fitted with the experimental data. The drag coefficient from the free-decay test in surge for the closed cage is $C_D = 0.8$. The value is much smaller than that for the semi-closed cage.

2.7. Sloshing modes

It is not straightforward to obtain the sloshing natural periods for a semi-closed cage analytically. Therefore, we make the assumption that they share similar values as those of a closed cage with similar dimensions and use them to analyze and interpret the experimental results. The reason is that the sloshing phenomenon inside a semi-closed cage is expected to resemble that in a closed cage for the examined wave conditions. Detailed results for the closed cage have been shown in Shen et al. (2021) and only the surface wave pattern of sloshing modes and corresponding natural periods T_{mn} are repeated here for illustration, as shown in Fig. 6. The sloshing natural period T_{mn} is defined in Faltinsen and Timokha (2009), where m is related to the mode shape $\cos m\theta$ (or $\sin m\theta$) and n numbers the infinite number of natural periods for each $\cos m\theta$ (or $\sin m\theta$).

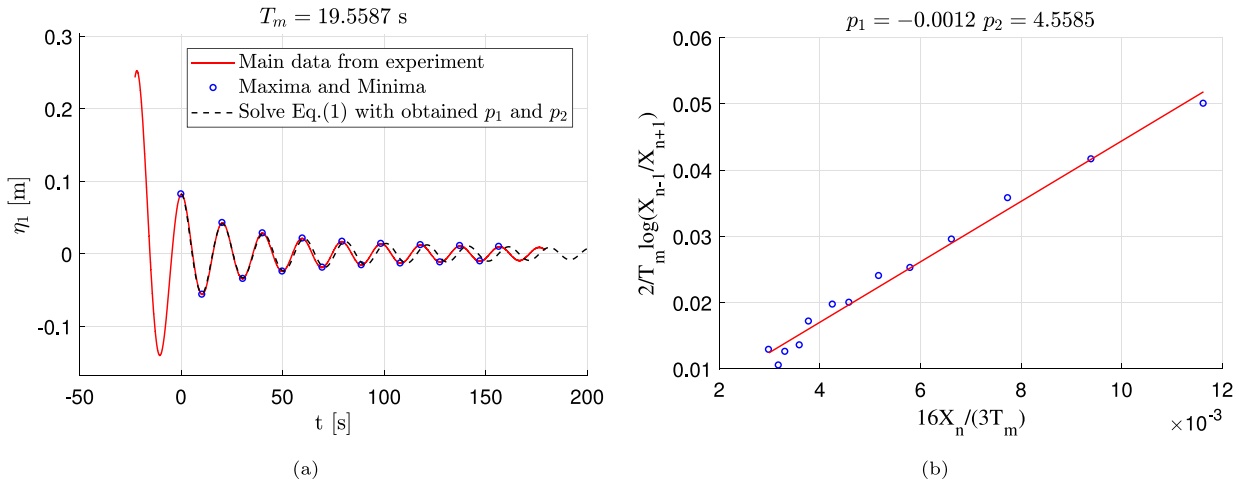

Fig. 5. (a) Red solid line: time history of surge motion from free decay test of the semi-closed cage in ambient calm water. Black dashed line: predicted surge based on Eq. (1). T_m is the mean natural period. (b) Illustration of how to obtain linear damping coefficient p_1 and quadratic damping coefficient p_2. X_n is the amplitude of the nth oscillation, based on the maxima and minima shown in the left plot.

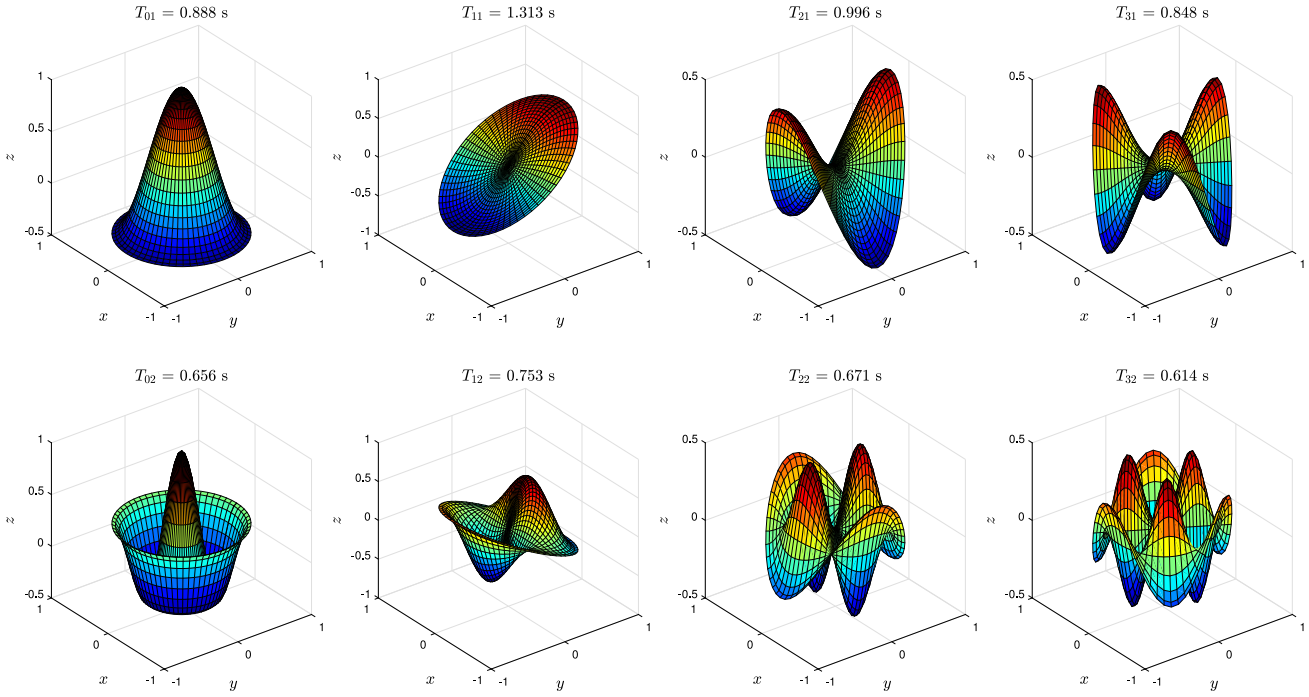

Fig. 6. Surface wave pattern of sloshing modes ($\cos m\theta$, $m = 0, 1, 2, 3$, $n = 1, 2$) and corresponding natural periods T_{mn} in a vertical circular tank with radius $R_t = 0.745$ m and water depth $h_t = 0.73$ m.

3. Experimental results and discussions: regular waves and white-noise waves

In this section, we will firstly show and discuss selected results from the model tests for the semi-closed cage in regular waves and white-noise waves. The focus is on transfer functions of the measured variables in the range of wave periods associated with local wind generated waves. Predictions from the linear potential flow solver WAMIT (Lee, 1995) are also provided, assuming a rigid structure. Comparisons between the closed and semi-closed cage for the different variables is given in the end of this section. The experimental accuracy in generating prescribed (regular and white-noise) waves has been assessed in Shen et al. (2021), so is omitted here.

3.1. Transfer function of rigid cage motions: semi-closed cage

As mentioned in Section 2.2, the motions of the semi-closed cage were measured with two methods, either using the eight markers along the cage side wall or obtained directly from the three-markers system. The former can provide both rigid motions and radial elastic deformations of the cage, while the latter can provide 6 DOF rigid body motions directly and is only applicable for rigid bodies. Fig. 7 shows the time histories of the surge, heave and pitch motions obtained from the two methods for the case with wave period $T = 1.02$ s, wave height $H = 0.027$ m and wave steepness $H/\lambda = 1/60$, corresponding to wavelength to cage diameter ratio $\lambda/D = 1.08$. The two measurements provide consistent results for heave and pitch motion. For surge, similar results are provided at the initial stage, but after about 50 periods, larger difference is observed when the waves associated with ovalizing

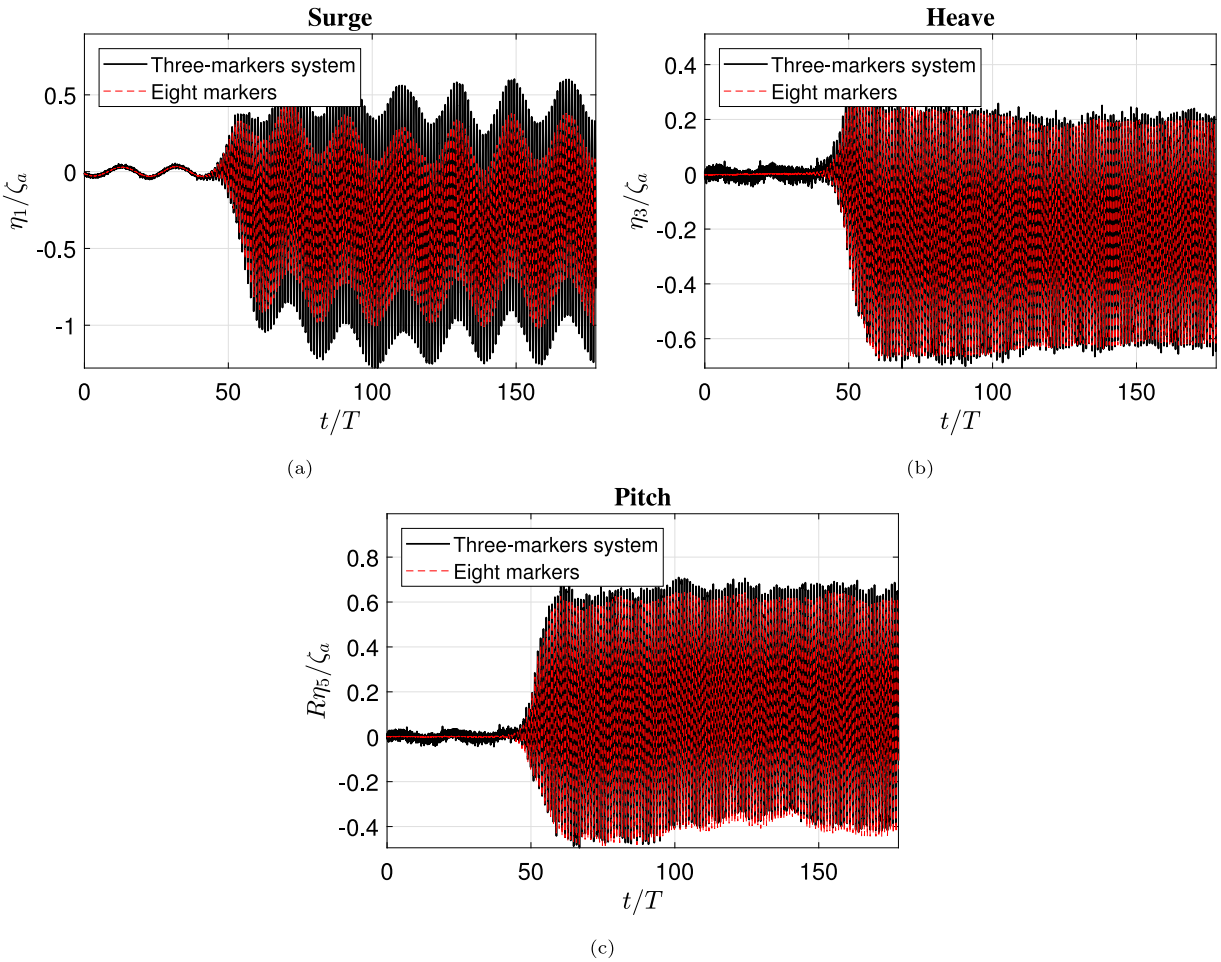

Fig. 7. Time histories of the surge, heave and pitch motions of the semi-closed cage. Solid black line: from the three-markers system. Dashed red line: from the distributed eight markers at the freeboard. $T = 1.02$ s, $H = 0.027$ m and $\lambda/D = 1.08$. $R = D/2$ is the outer radius of the semi-closed cage.

structural deformation modes inside the cage become high in time. A more detailed comparison of the rigid body motions from the two measurements for different wave periods was performed (not provided here), showing that the two approaches provide consistent results for all cases, except for the surge motion at wave periods close to the sloshing natural period T_{21} where the cage experiences large ovalization deformations. The rigid body motions from the eight markers will be used for further analysis.

It should be noted that there is a mean negative heave (positive sinkage) for the case shown in Fig. 7(b), which was not observed for the closed cage, as documented in Shen et al. (2021). Because of the used mooring-line set-up, the influence of mooring lines on this mean sinkage (due to possible nonlinear stiffness effects) is expected to be negligible. To have a better understanding of this effect, the mean heave motion is shown in Fig. 8 as a function of λ/D. Results from two repetition tests are included. The results are consistent, indicating that the sinkage is not caused by leakage of the floating collar and is repeatable. In the figure, the values are made non-dimensional in two ways, i.e. by the cross-sectional radius of the floater collar r_f (see Fig. 8(a)) and by the square of the incident wave amplitude ζ_a^2 (see Fig. 8(b)). Excluding the results in short incident waves, Fig. 8(b) shows that the mean sinkage is almost proportional to the square of the incident wave amplitude, which denotes that it is related with nonlinear behavior (at least second-order wave-body interaction effects) of the cage. The large deviations in shorter waves are due to small incident wave amplitude. A possible reason for the sinkage is the water overtopping on the floating collar, as observed from the recorded videos. Here, this phenomenon indicates that external water reaches the top of the floater. Because the freeboard of the experimental cage is much higher than that of the floater, the water cannot enter the cage when overtopping occurs. Fig. 8(a) shows that the mean sinkage increases with increasing wave period and wave steepness, with a maximum sinkage up to $0.7r_f$. Since the restoring stiffness for pitch motion is mainly provided by the floating collar, it is expected that the behavior of the oscillatory pitch motion may be altered due to the large change of mean draft, especially in longer waves.

Fig. 9 shows the transfer functions for surge, heave and pitch in a frequency range of primary importance for local wind generated waves. Experimental data from regular waves and the two white-noise tests are given. Results from the linear potential-flow solver WAMIT are also provided, assuming the floating collar is half-submerged when in calm water. Motion amplitudes for surge and pitch from regular waves, in general, agree reasonably with those from the white-noise tests in shorter waves (λ/D <1.5), but there is an increasing difference in longer waves. This may be caused by the change of mean draft and the resulting nonlinear effects. Different wave steepness (for regular waves) and different significant wave height (for white noise waves) give different transfer functions for heave even in shorter waves, indicating the importance of nonlinear effects for the heave motion.

Important sloshing natural periods $T_{21} = 0.996s$ and $T_{12} = 0.753s$ in model scale for the closed cage are denoted with vertical dashed lines in the figure. Surface wave pattern of the corresponding three sloshing modes were exemplified in Fig. 6. The sloshing induced wave would not feel the cage bottom if the corresponding draft-to-wavelength ratio $h/\lambda > 1/2$ or $\lambda/D < 1$ for the present case where $h/D = 1/2$. This means that the natural sloshing periods T_{21} and T_{12} should be similar for the

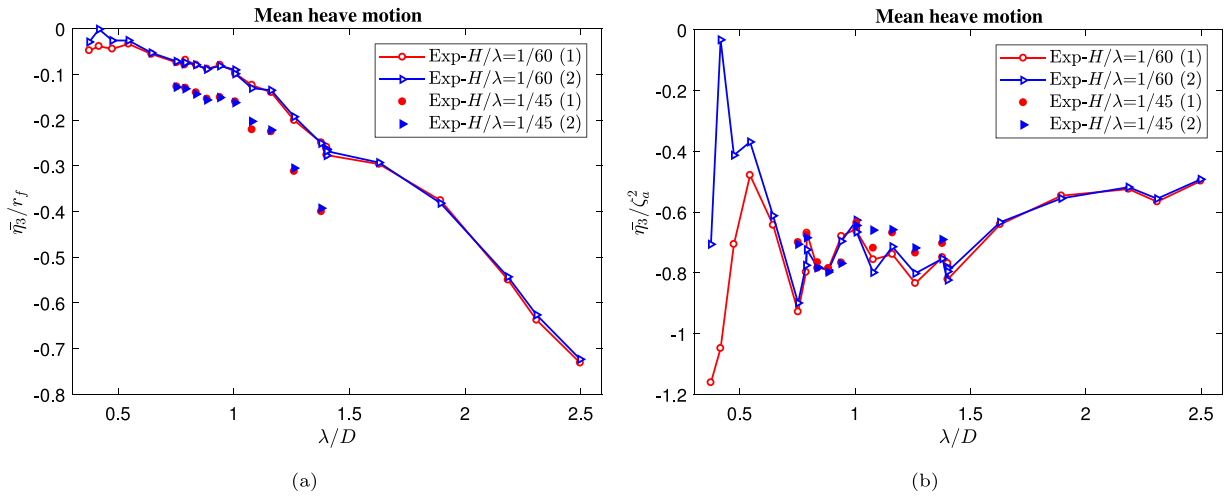

Fig. 8. Non-dimensional mean heave versus wavelength-to-cage diameter ratio λ/D. (a): made non-dimensional by cross-sectional radius of the floating collar r_f. (b): made non-dimensional by the incident wave amplitude squared, i.e. ζ_a^2. Two wave steepnesses λ/D = 1/60 and 1/45 are examined. Results from two repetition tests are included.

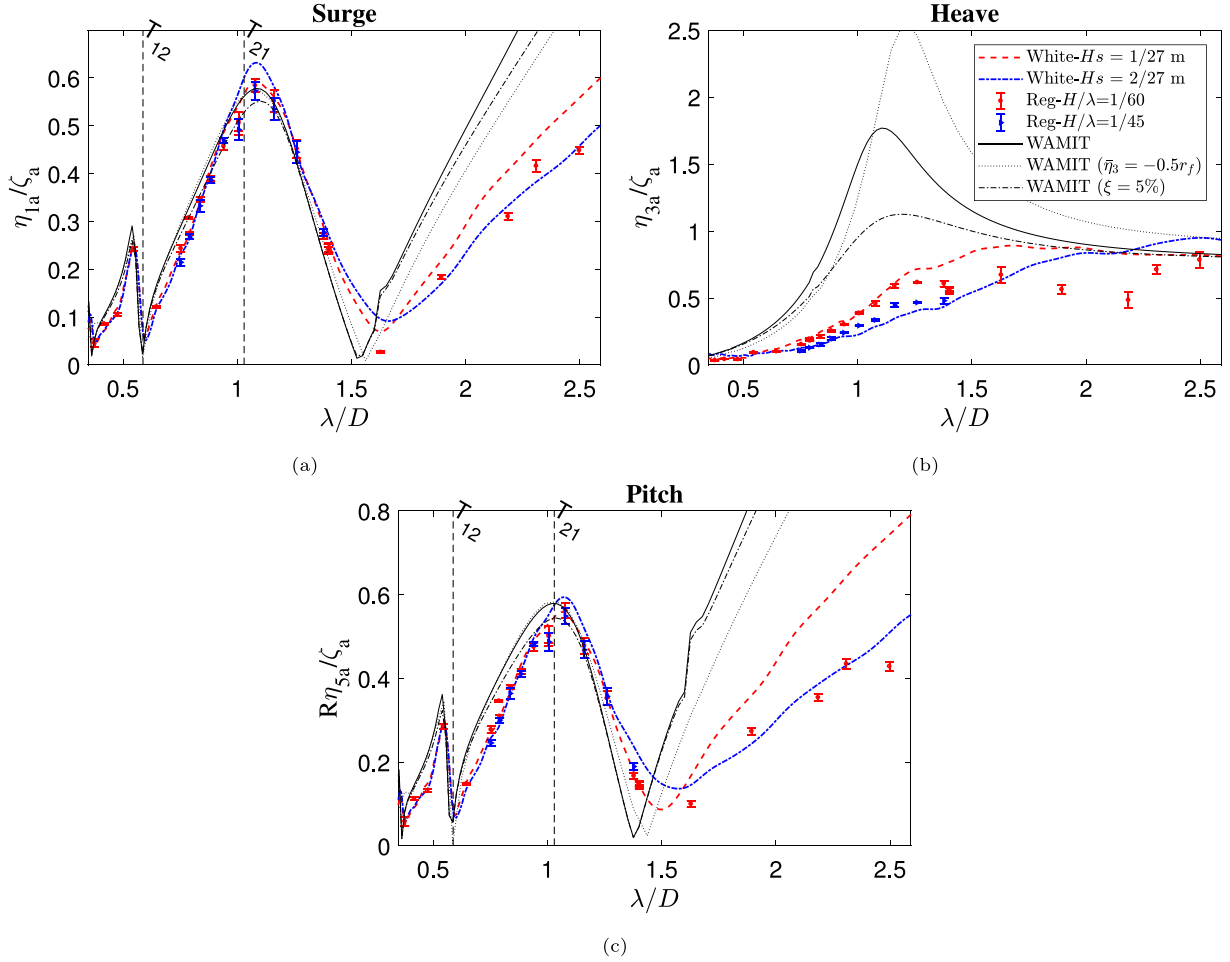

Fig. 9. Experimental and numerical transfer functions of surge, heave and pitch versus wavelength-to-cage diameter ratio λ/D. ζ_a is the incident wave amplitude. Black solid lines: WAMIT calculations when the cage is at rest. Black dotted lines: WAMIT calculations with mean heave sinkage = $0.5r_f$. Black dash-dotted lines: WAMIT predictions with added damping = 5% of critical damping. T_{ij} = natural sloshing periods for a closed cage (see Fig. 6).

two cages. For the closed cage in Shen et al. (2021), nearly zero surge happens at $\lambda/D = 1.794$ (corresponding to $T = T_{11}$). If surge motion is uncoupled with the other rigid body motions, zero surge motion will happen theoretically at T_{11} due to infinite surge-added mass associated with potential flow sloshing (Faltinsen and Timokha, 2009). For the open cage, nearly zero surge happens at $\lambda/D = 1.55$.

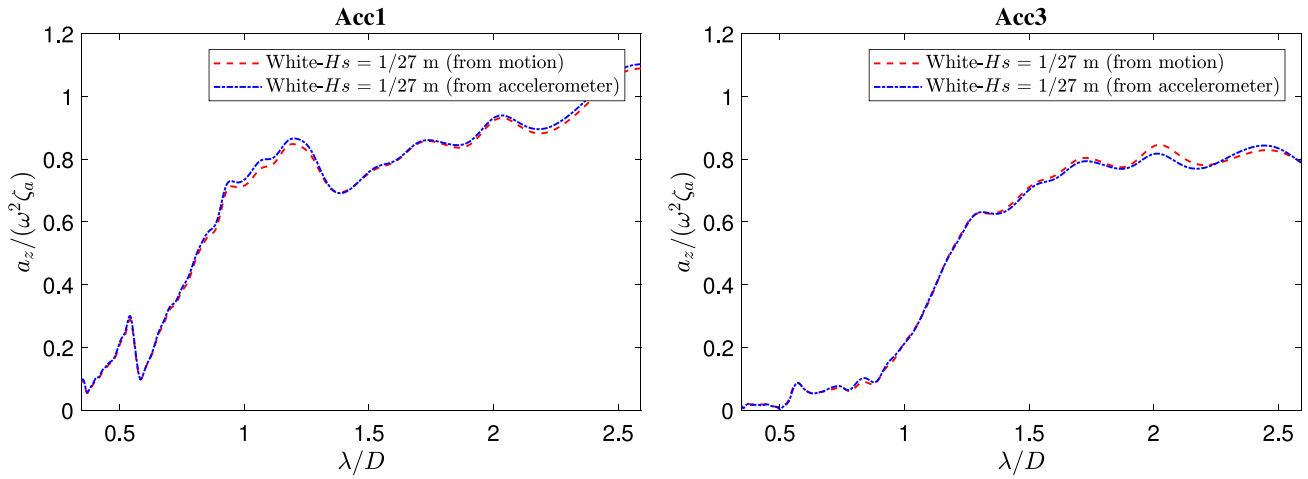

Fig. 10. Comparison of the non-dimensional vertical acceleration from accelerometers and from rigid body motions. Left: at accelerometer Acc1. Right: at accelerometer Acc3.

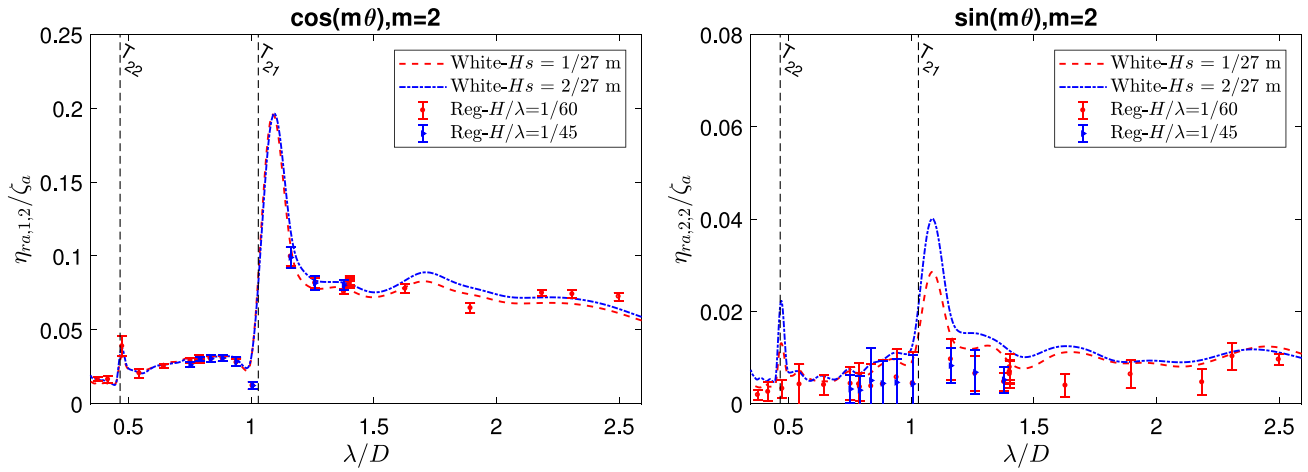

Fig. 11. Transfer function of the radial deformation of the ovalizing modes $\cos(2\theta)$ and $\sin(2\theta)$ of the open-bottom cage measured at the freeboard level versus wavelength-to-cage diameter ratio λ/D. The data are based on experiments in either regular or truncated white-noise waves. T_{21} and T_{22} = natural sloshing periods for ovalizing modes.

There is overall a good agreement between WAMIT and the experimental surge and pitch transfer functions in shorter waves (λ/D <1.5). The large difference in longer waves is caused by the nonlinear effects in the wave-body interactions in these conditions. For the heave motion, linear potential flow theory is not adequate. Numerical calculations with an increase of the draft by $0.5r_f$ have been also performed, providing slightly better predictions of surge and pitch. The reason to choose an increase of draft by $0.5r_f$ is that the maximum sinkage of the cage is about $0.5r_f$ in waves with $\lambda < 2D$. Therefore, this choice can help us to assess the influence of cage sinkage on the body motions and its role on the discrepancies between numerical and experimental results. Significant improvement of the WAMIT prediction for heave motion is achieved near the resonance zone by adding a linear damping that equals 5% of the critical damping, suggesting importance of viscous damping connected with flow separation. Nevertheless, the influence is small on the surge and pitch motion as the examined wave periods are still far from the corresponding natural periods.

Accelerations obtained from accelerometers could serve as a check for the measurements of the rigid body motions obtained from the eight markers. The transfer function of vertical acceleration $H_{a,z}$ at a given point (x, y, z) on the cage wall can be estimated based on the transfer functions of rigid body motions, following

$$H_{a,z}(\omega) = -\omega^2\left[H_{\eta_3}(\omega) + yH_{\eta_4}(\omega) - xH_{\eta_5}(\omega)\right] \quad (2)$$

where H_{η_3}, H_{η_4}, and H_{η_5} are complex transfer functions of heave, roll and pitch motion, respectively. ω is the (circular) frequency of the incident waves. The comparison of non-dimensional vertical accelerations from two accelerometers (Acc1 and Acc3 defined in Fig. 4) and from Eq. (2) is documented in Fig. 10, confirming a good agreement.

3.2. Transfer function of radial elastic deformations: semi-closed cage

Both rigid body motions and elastic deformations can be extracted from the measurements of the eight markers installed at the freeboard of the cage (Shen et al., 2021). Fig. 11 presents the transfer functions of the ovalizing modes $\cos 2\theta$ and $\sin 2\theta$ in the radial direction of the semi-closed cage at z = 0.35 m from both the regular wave tests and the white-noise tests. The ovalizing mode $\sin 2\theta$ is caused partly by structural asymmetry. The peak deformation occurs at λ/D = 1.078 (T = 1.018 s) for both modes, close to the corresponding sloshing natural period T_{21}=0.996 s, as a consequence of coupling between structural ovalizing modes and corresponding sloshing modes. A numerical analysis of the ovalizing modes for the closed cage was attempted in Shen et al. (2021) by combining a structural software with WAMIT. The resonant frequencies in model tests were captured relatively well by the numerical model. Similar approach can be applied for the present semi-closed cage and is left as future work.

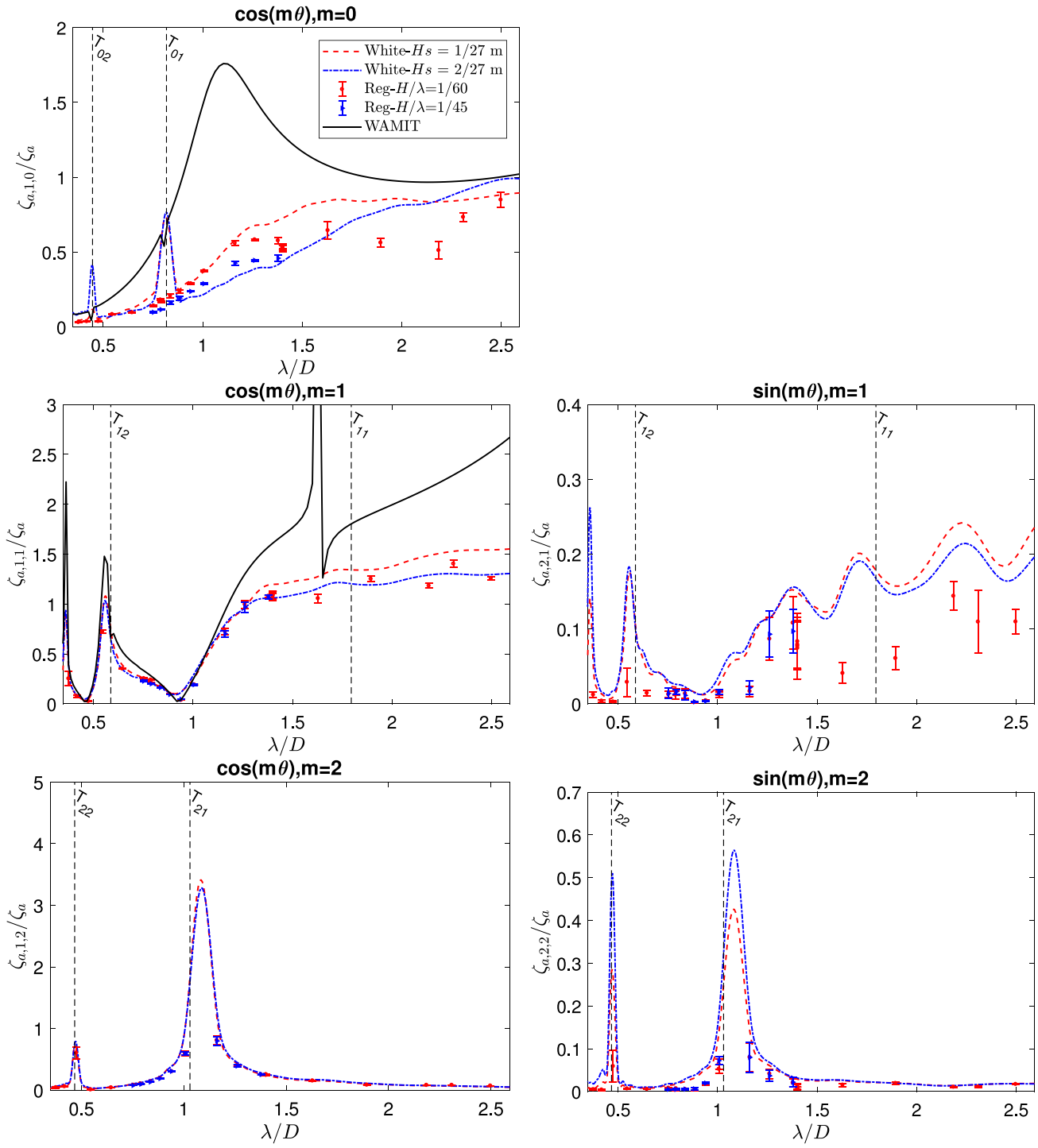

Fig. 12. Transfer function of the interior-wave modes $\cos m\theta$ (left) and $\sin m\theta$ (right) for the open-bottom cage measured at $r = 0.95R$. Top: $m = 0$. Middle: $m = 1$. Bottom: $m = 2$. Results from WAMIT for $\cos m\theta (m = 0, 1)$ modes are also provided for comparison. T_{mn}= natural sloshing period associated with $\cos m\theta$ (or $\sin m\theta$) free-surface mode dependence.

3.3. Transfer function of interior waves: semi-closed cage

Free-surface elevation inside the container was measured by the eight interior wave probes RW1-8, see Fig. 4. The probes were fixed to the cage, so the measured values are related to the tank-fixed coordinate system. To better relate the interior wave elevation with sloshing modes, the Fourier components $\cos m\theta$ and $\sin m\theta$ of the internal waves are calculated at $r = 0.95R$, based on the method explained in Shen et al. (2021), by using measurements of eight interior wave probes. Transfer functions of the first three $\cos m\theta, m = 0, 1, 2$ modes and the first two $\sin m\theta, m = 1, 2$ modes are presented in Fig. 12. Relevant sloshing natural periods for different modes are indicated by the vertical dashed lines. There is only $\cos m\theta$ $(m = 0, 1)$ component according to linear rigid-body theory. Numerical predictions based on linear potential-flow solver WAMIT are also provided, considering only rigid-body motions. WAMIT provides poor prediction of $\cos m\theta$ $(m = 0)$ component due to poor prediction of heave motion. Reasonable agreement with the experimental results is achieved for $\cos\theta$ mode in shorter waves $(\lambda/D < 1.2)$, but not for longer waves due to poor prediction of pitch motion (see Fig. 9(c)). The modes $\cos 2\theta$ and $\sin 2\theta$ are associated

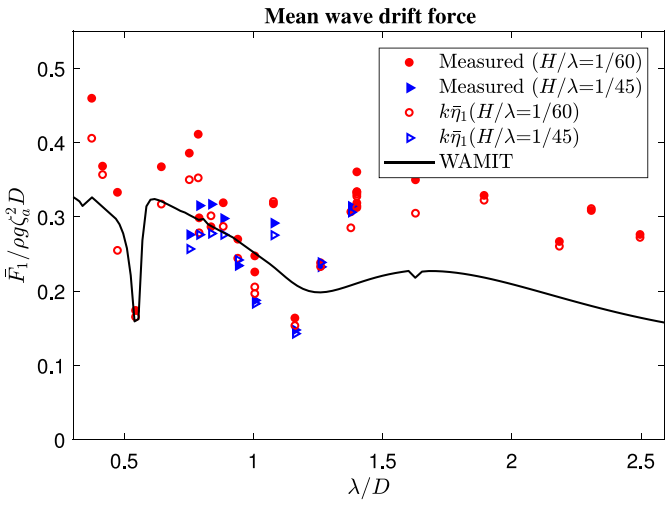

Fig. 13. Non-dimensional mean wave drift force $\bar{F}_1$ in x-direction versus λ/D. Solid symbols: from tension measurement. Open symbols: from mean surge motion. Solid line: from WAMIT. Two wave steepnesses $H/\lambda = 1/60$ and $1/45$ are included.

with structural ovalizing deformations, so they cannot be captured by WAMIT.

3.3.1. Mean wave drift forces: semi-closed cage

Mean wave drift loads are important for performing mooring lines analysis. In Shen et al. (2021), we proposed two ways to estimate the mean wave-drift force in surge: (1) from tension measurement of the mooring lines; (2) by multiplying the mean surge motion with the equivalent linear stiffness k_s of the system. Both results are shown in Fig. 13. Possible reasons for the difference between the two approaches were explained in Shen et al. (2021). Predictions based on linear potential-flow solver WAMIT are also provided in the figure. The option to remove irregular-frequency effects was used during the calculations. The asymptotic value of $\bar{F}_1/\rho g\zeta_a^2 D$ is 1/3 for $\lambda/D \to 0$, according to second-order potential flow theory (see Faltinsen (1993)). This is in good agreement with WAMIT. The larger difference in longer waves ($\lambda/D > 1.5$) is related with WAMIT's poor prediction of rigid body motions, as shown in Fig. 9. Also, the small thickness of the open-bottom cage side wall makes it difficult to perform accurate WAMIT calculations and refined mesh near the free surface is needed to give reliable predictions.

3.4. Transfer functions: semi-closed cage versus closed cage

In this section, detailed comparisons of transfer functions between the semi-closed and closed cage are performed. The examined variables are rigid body motions, radial elastic deformations, interior waves and mean wave drift loads.

3.4.1. Rigid body motions

Transfer functions of rigid body motions from the white-noise test WH-1 are shown in Fig. 14. A wide region of wave lengths is examined. From Fig. 14(a), the two cages have similar surge behavior in shorter waves ($\lambda/D < 1$). The reason for the similarity is that the incident waves would nearly not feel the cage bottom if the draft-to-wavelength ratio $h/\lambda > 1/2$ or $\lambda/D < 1$ for the present case where $h/D = 1/2$. Both cages have a local peak close to the corresponding pitch natural period, due to the coupling between surge and pitch. From Fig. 14(c), similar behavior is observed for pitch in shorter waves ($\lambda/D < 1$), with the semi-closed cage exposed to larger pitch motion. A possible reason is that the semi-closed cage has smaller metacentric height, i.e. it is less stable. The maximum pitch for the semi-closed cage occurs at wave period slightly larger than the pitch natural period $T_{n,5,o}$ from the free-decay test, while it happens at the exact natural pitch period $T_{n,5,c}$ for the closed cage. A possible reason is that the natural pitch period for the semi-closed cage is altered due to the in and out of water motion of the floating collar. This will happen only in very severe sea state for the closed cage (Shen et al., 2021). From Fig. 14(b), the closed cage experiences very small heave motion in shorter waves ($\lambda/D < 2$) and a clear resonance is observed at its natural period $T_{n,3,c}$. The semi-closed cage displays a very peculiar behavior. No clear resonance is observed. A local trough occurs at $\lambda/D = 4.26$, which is associated with moonpool piston resonance. According to Molin et al. (2018), the natural frequency of piston resonance ω_{00} for a circular moonpool in finite water depth can be estimated as

$$\omega_{00}^2 = \frac{g}{h + 4\sum_{n=1}^{\infty} \frac{J_1^2(\lambda_n R_t)}{\lambda_n^3 R^2 \tanh(\lambda_n c) J_1^2(\lambda_n R)}} \tag{3}$$

where J_m is the Bessel function of the first kind of order m, λ_n is the nth root of $J_0(\lambda_n R) = 0$, h is the cage draft and c is the clearance between the cage bottom and the ocean basin floor. R and R_t are the outer and inner radius of the moonpool. The influence of the bottom buoyancy element in our cage is expected to be small and is neglected in this estimation. The piston resonance occurs at wavelength-to-diameter ratio $\lambda/D = 4.13$ according to Eq. (3) . The value is quite close to the experimentally obtained value $\lambda/D = 4.26$.

3.4.2. Radial elastic deformations

Fig. 15 presents a comparison of the ovalizing deformations between the closed and semi-closed cage. The transfer functions are obtained from the white-noise test WH-1. There is a small difference between the two cages for the $\cos 2\theta$ mode, even at the resonant period. This demonstrates that the open bottom has a small influence on this mode. The large difference for the $\sin 2\theta$ mode for the two concepts is probably due to that the semi-closed cage has less asymmetry with respect to the x-axis compared with the closed one. The asymmetry of the closed cage mainly comes from the steel stiffened tubes installed at the bottom (documented in Shen et al. (2021)), which are not present for the open bottom cage.

3.4.3. Interior waves

A comparison between the different interior wave modes of the closed and semi-closed cage is shown in Fig. 16 for a wide range of wave periods. Relevant results are from the white-noise test WH-1. The two cages display similar trend for $\cos m\theta$ and $\sin m\theta$ ($m = 1$) modes in shorter waves ($\lambda/D < 1$). The $\sin m\theta$ ($m = 2$) modes for the closed cage are larger than those for the semi-closed cage, due to stronger structural asymmetry with respect to the $x - z$ plane, as the former was equipped with asymmetric steel stiffened tubes at the bottom. For modes $m = 2$, the obtained wave modes are correlated with those for the structural ovalizing deformations (compared with Fig. 15). A clear peak is observed for the mode $\cos m\theta$ ($m = 0$) at $\lambda/D = 4.77$ due to combined effect of heave motion and piston resonance. For mode $\cos m\theta$ ($m = 1$), which is related with the surge and pitch motions, the local peaks occur at similar locations as those for the pitch motion (compared with Fig. 14).

3.4.4. Mean wave drift loads

Fig. 17 shows the comparison of the mean drift forces in surge from the regular-wave tests for the semi-closed and closed cages. The mean surge forces were estimated by multiplying the mean surge motion with equivalent linear stiffness of the system. The general trend and the force values are similar for the two cages. This demonstrates that whether the cage has bottom or not has small influence on the mean wave drift loads for the examined wave periods.

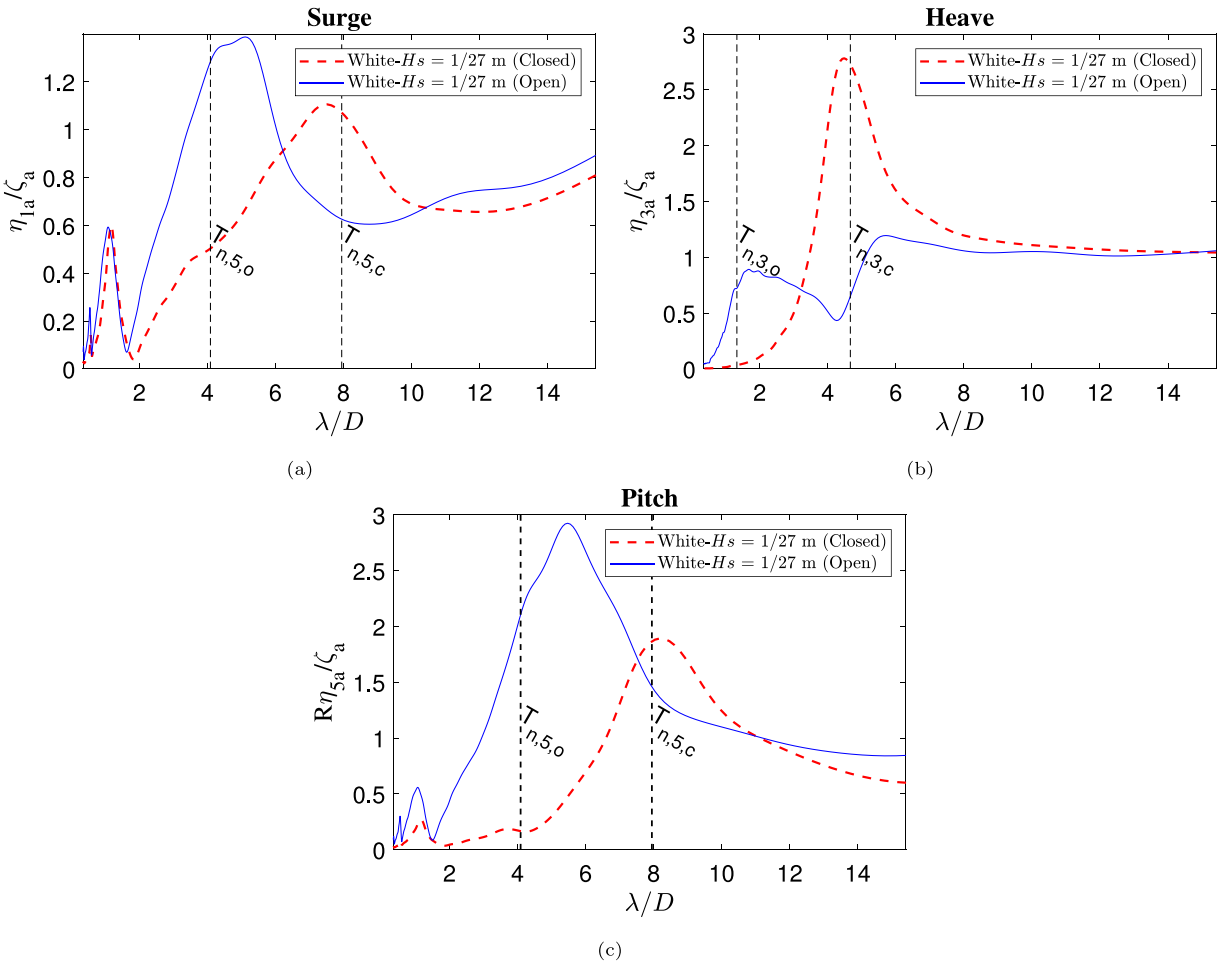

Fig. 14. Transfer functions of surge, heave and pitch versus wavelength-to-cage diameter ratio λ/D for the closed cage and the semi-closed cage. Experimental results are from the white-noise wave WH-1 with H_s = 1/27 m. Red dashed line: closed cage. Blue solid line: semi-closed/open-bottom cage. $T_{n,3,o}$ and $T_{n,5,o}$ are, respectively, the natural periods in heave and pitch from free decay tests for the semi-closed cage. $T_{n,3,c}$ and $T_{n,5,c}$ are the corresponding natural periods for the closed cage.

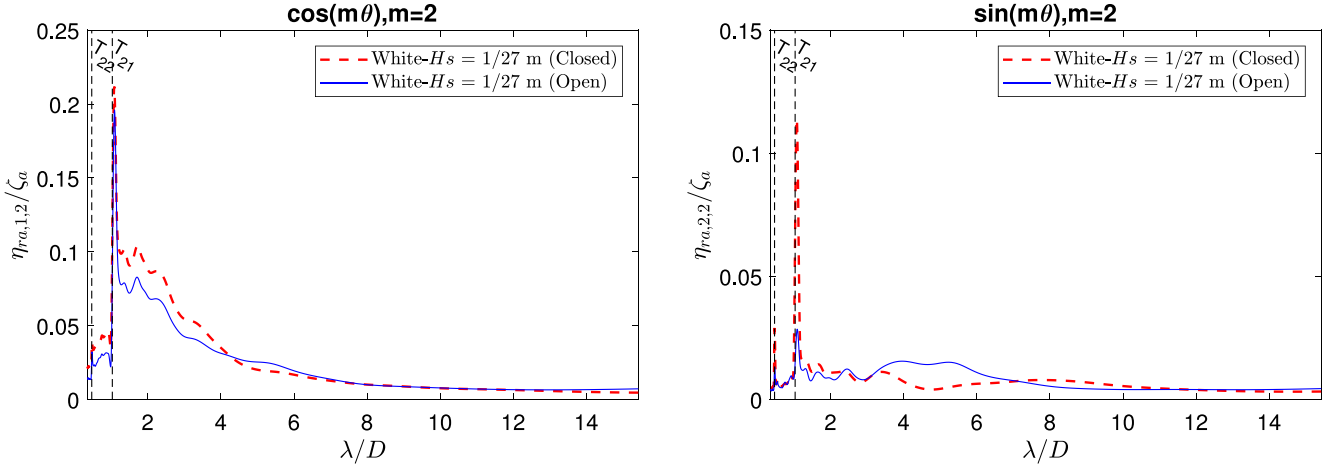

Fig. 15. Comparison of the radial deformations of ovalizing modes between the closed cage and open-bottom cage in a wider range of wave periods. Closed cage: red dashed line. Open-bottom cage: blue solid line. The data are from experiments in white-noise waves.

4. Experimental results and discussion: irregular waves

To better understand the behavior of the semi-closed and closed cages in realistic sea conditions, model tests for both cages in irregular seas were also performed and they are discussed in this section. The experimental accuracy in the generation of prescribed irregular waves is assessed at first. Then, examples of the time histories of the different variables, measured in the tests with random-time realizations of the examined sea states, and the corresponding power spectral distributions are provided. Statistical analysis is also performed. In the end, empirical approaches to estimate the standard deviation of different variables based on available transfer functions are proposed. All the results given

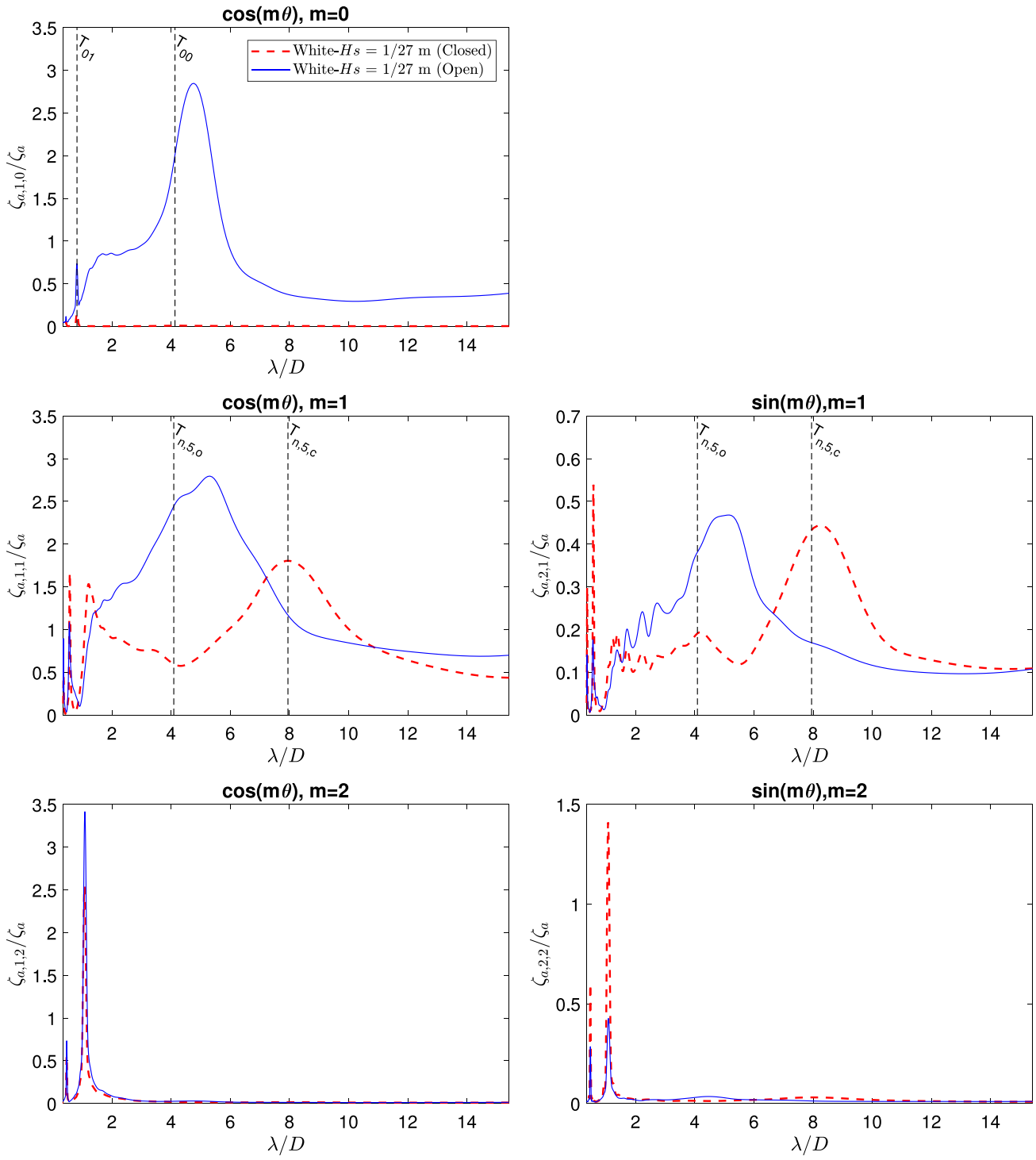

Fig. 16. Same as in Fig. 12, but with the comparison between the closed cage (red dashed line) and open-bottom cage (blue solid line).

hereafter are in full-scale, so to provide a practical idea of the obtained values.

4.1. Incident wave

Two tests with incident waves generated according to the JONSWAP spectrum were performed, see Table 4. As an example, the time history of the incident irregular wave IRR-2 is provided in Fig. 18(a). The prescribed significant wave height is $H_s = 2$ m, the peak wave period is $T_p = 6s$ and the spectral peakedness is $\gamma = 2.39$, corresponding to high exposure sea state in Table 1. Fig. 18(b) presents a comparison of the wave spectrum derived from irregular waves generated experimentally and the prescribed JONSWAP wave spectrum. This confirms a reasonable agreement and documents a wave-frequency energy between about 0.1 and 0.4 Hz, corresponding to wave periods between 2.5 and 10 s, for these irregular waves. The actual measured incident-wave parameters are used in the actual analysis of the data. However, for convenience the prescribed incident-wave parameters are used in the figures captions and in the main text.

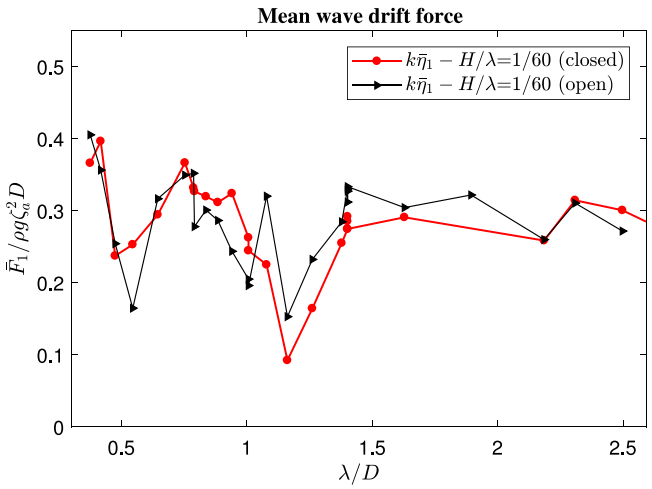

Fig. 17. Comparison of the mean surge force from the model tests for the closed and open-bottom cage. The examined wave steepness is $H/\lambda = 1/60$.

4.2. Examples of time histories

Fig. 19 shows examples of time histories of surge, heave, pitch and interior wave elevation (wave probe RW4, defined in Fig. 4) for the case IRR-2 with H_s =2 m and T_p = 6 s. Results for the closed and semi-closed cage are included for comparison. For surge, the slowly varying component is dominant for both cages. For heave, the semi-closed cage has much smaller minimum values than the closed cage, but has similar peak values. A clear sinkage of the semi-closed cage is observed due to possible overtopping at the floater and in and out of water motion of the floater, similarly as in regular waves. For pitch, the semi-closed cage has larger standard deviation, but has similar minimum and maximum values as the closed cage. For wave probe RW4, both the phases and amplitudes of the measured wave elevations are similar for the two cages.

Fig. 20 presents the corresponding power spectra of the time histories given in Fig. 19. The slowly varying component for surge motion (with natural period greater than 100 s) is dominant for both cages, and is not included in the figure, by limiting the x-axis within 3–20 s, so to highlight the other contributions. For pitch, there is an important contribution outside the incident wave frequency range, in particular at periods larger than the incident-wave periods, for both cages. This is caused by nonlinear interaction between the incident wave and the cage, more specifically due to the nonlinear difference-frequency excitation. For the closed cage the peak of this low-frequency component occurs at wave period close to the corresponding pitch natural period $T_{n,5,c}$, while for the semi-closed cage the peak happens at about $2T_{n,3,o}$ instead of near the pitch natural period $T_{n,5,0}$. One should note that $T_{n,5,o}$ is the value of the pitch natural period estimated from the free-decay tests. So, a possible reason is that the water-entry and water-exit phases of the floating collar would change the natural period of pitch. A similar phenomenon was observed in Shen et al. (2021) for the closed cage. For wave probe RW4, the wave elevation inside the closed cage (see Fig. 20(a)) basically coincides with the corresponding pitch induced vertical motion at wave periods close to the natural pitch period. The reason is that there is a negligible incident-wave energy at such wave periods, so the main contribution of the interior wave comes from the pitch induced vertical motion. For the open-bottom cage (see Fig. 20(b)) the wave probe measurement for wave periods close to $2T_{n,3,o}$ is less than 50% of the corresponding pitch induced displacement. The difference is due to an additional contribution to the interior wave coming from the interior piston-mode flow, which counteracts the pitch induced displacement.

4.3. Statistical analysis

A statistical analysis is given in this section for the different measured variables.

4.3.1. Rigid body motions

Fig. 21 presents the comparison of the mean $\bar{\eta}_i$, standard deviation σ_{η_i}, maximum $\eta_{i,max}$ and minimum $\eta_{i,min}$ values of the rigid body motions, with $i = 1, 3, 5$ corresponding to surge, heave and pitch motion, respectively. One should note that $R\eta_5$ instead of η_5 is used in the analysis to have consistent unit for all motions and that the mean value has been subtracted from the plotted maximum and minimum values.

From Fig. 21(a), the two cages have comparable mean surge motion $\bar{\eta}_1$, which is intuitively reasonable as the corresponding transfer functions of mean wave-drift loads in surge are similar (see Fig. 13). The closed cage possesses slightly larger standard deviation σ_{η_1} due to smaller viscous damping. From Fig. 21(d), the ratios $\eta_{1,max}/\sigma_{\eta_1}$ and $|\eta_{1,min}|/\sigma_{\eta_1}$ vary between 3–4.

From Fig. 21(b), the closed cage has small heave motion, so this motion is not of interest. For the open cage, a clear mean sinkage is observed due to continuous water overtopping on the floating collar, similarly as in regular waves. From Fig. 21(e), there is an asymmetry of the motion with much smaller $\eta_{3,max}$ than $|\eta_{3,min}|$. The ratio $|\eta_{3,min}|/\sigma_3$ approaches 6 due to nonlinear behavior of the system.

From Fig. 21(c), the open cage in general experiences larger pitch motion than the closed one. There is also a small mean positive pitch. The ratio $|\eta_{5,min}|/\sigma_{\eta_5}$ could get close to 8 (see Fig. 21(f)) for the closed cage in irregular wave IRR-2. The reason is that the standard deviation for the closed cage is smaller than for the open one, but the values of $|\eta_{5,min}|$ for the two cages are similar, as shown in Fig. 19.

4.3.2. Interior wave elevation

Similar as in Fig. 21, we examine the mean, standard deviation, maximum and minimum values of the interior wave elevation from the three interior wave probes (defined in Fig. 4) in Fig. 22. There is a mean positive value for the different wave probes for the semi-closed cage. This is connected with the sinkage of the cage documented in Fig. 8. Both the standard deviations and maximum values from the different wave probes are comparable for the two cages. The ratio between the maximum value and the standard deviation is close to 4 for most of the cases, which is a typical value for a stationary Gaussian process wave, except for the wave probe RW4 in irregular wave IRR-2 for both cages, for which the ratio is close to 6.

To better understand the reason for this exception, we examine the closed-cage case. In Fig. 23(a), we show the time history of the measured wave elevation at RW4 for the case IRR-2. Time history of the incident wave is also included for illustration. The chosen time interval includes the time instant when the largest interior wave elevation occurs. Time histories of the different sloshing modes that contribute to the total wave elevation are shown in Fig. 23(b). From the figure, modes $\cos\theta$ and $\cos 2\theta$ are the two dominant components. The former is associated with the rigid body motions while the latter can only be excited by the ovalizing deformations. The maximum value occurs at t = 7972 s where the two dominant modes are in phase while they are 90° out of phase in the following trough. Strong nonlinearities are involved due to the large incident waves with the characteristic wave period close to the coupled sloshing-surge-pitch natural period and natural period of ovalizing deformations (see snapshots shown in Fig. 24 from the front camera). The nonlinear features of the rigid-body motions and interior waves induced by ovalizing deformations contribute to the large maximum value-to-standard deviation ratio at RW4.

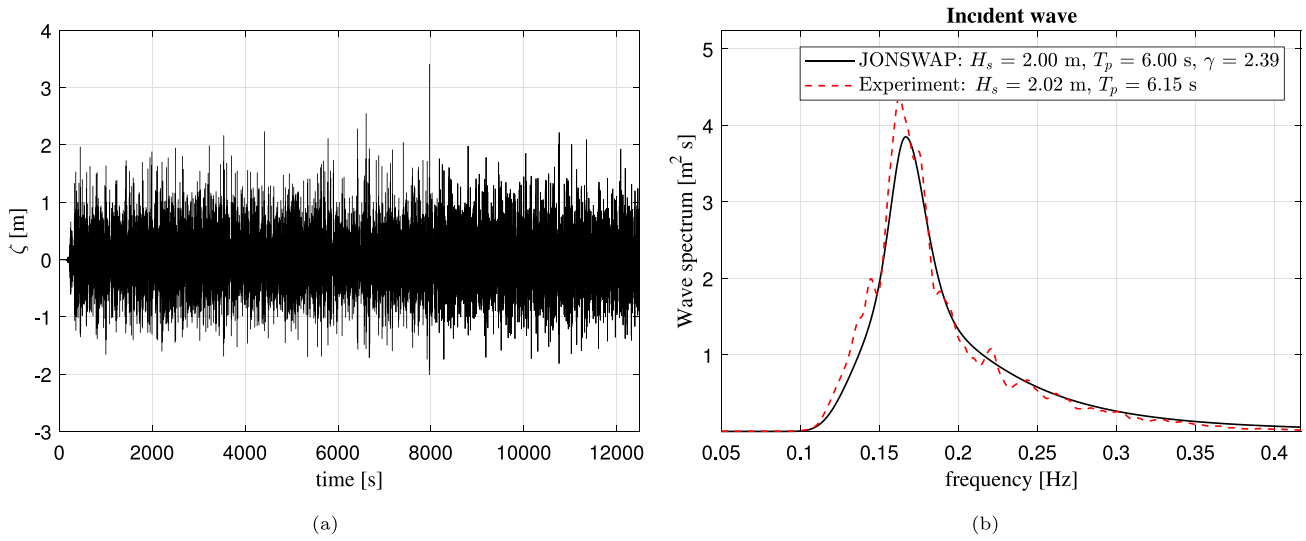

Fig. 18. (a): time history of incident wave ζ from Jonswap spectrum with prescribed full-scale significant wave height H_s =2 m and peak wave period T_p = 6 s. (b): comparison of wave spectral density from the experiment with the theoretical value.

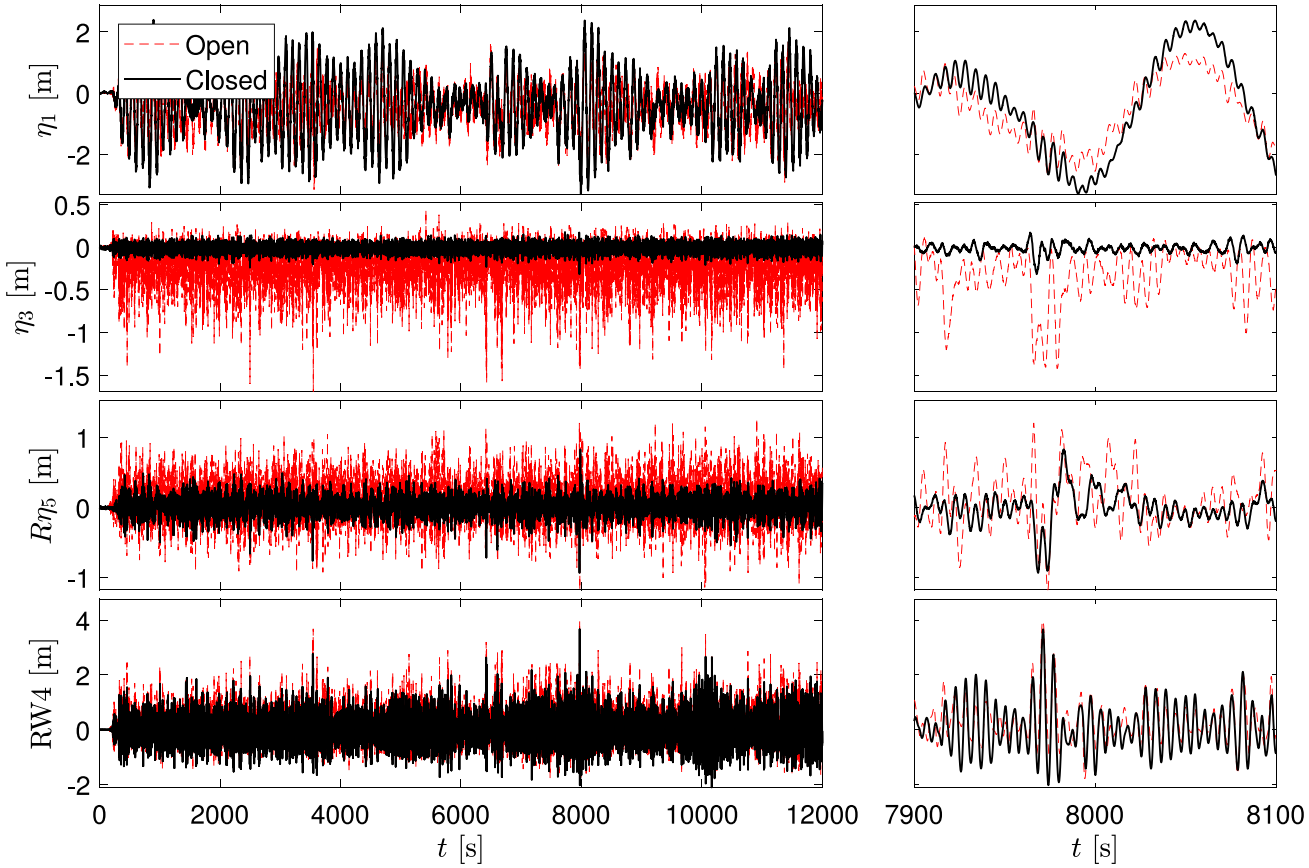

Fig. 19. Full-scaled experimental time histories of surge (first row), heave (second row), pitch (third row) motions and wave elevation from wave probe RW4 (last row). The prescribed incident-wave parameters are T_p= 6 s and H_s = 2 m. Zoomed views are also given in the right. Red dashed line: open-bottom cage. Black solid line: closed cage.

4.4. Numerical predictions

There is no doubt that the above introduced experimental results are interesting and enlightening, but they are just for limited sea states. To provide practical guidance for the cage design and operation, empirical estimations are needed. In this section, we try to propose empirical approaches to evaluate the standard deviation of different measured variables, which are used in Section 5 to determine the operational conditions for the two cages. Following the commonly-used engineering practice, the cages are assumed to behave like linear systems. In this way, linear superposition principle is valid and the desired standard deviations could be obtained based on obtained transfer functions either from the white-noise tests or from WAMIT calculations. The assumption may not be strictly true, especially for heave and pitch motions for the semi-closed cage, but it is still valuable to check the accuracy of the results based on such assumptions.

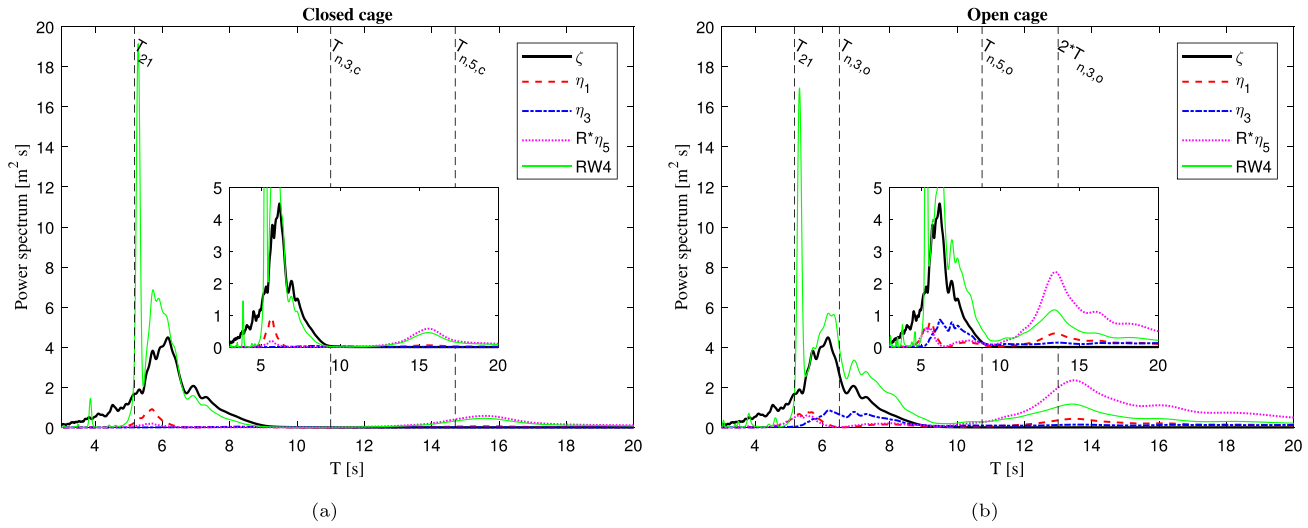

Fig. 20. Estimated power spectra of the different measured variables shown in Fig. 19. The power spectrum for the incident wave ζ is also included. Left: closed cage. Right: open-bottom cage. $T_{n,3,o}$ and $T_{n,5,o}$ are, respectively, the natural periods in heave and pitch from free decay tests for the semi-closed cage. $T_{n,3,c}$ and $T_{n,5,c}$ are the corresponding natural periods for the closed cage.

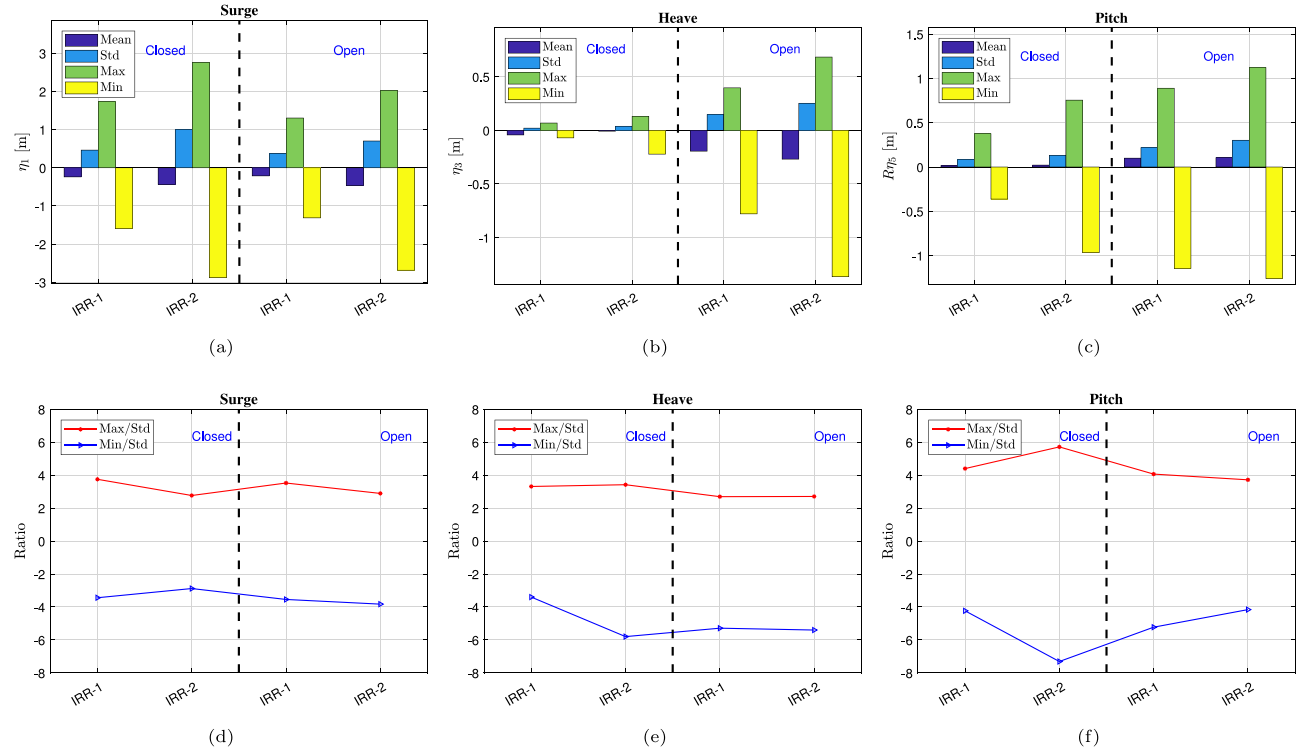

Fig. 21. (a)–(c): mean, standard derivation, maximum and minimum value of surge, heave and pitch motions in irregular waves. (d)–(f): ratios of the corresponding maximum and minimum value to the standard deviation. In each subplot, the left two cases are for the closed cage and the right two cases are for the open-bottom cage, separated by a vertical dashed line. IRR-1: T_p = 5 s, H_s = 1.5 m and γ = 2.87. IRR-2: T_p = 6 s, H_s = 2.0 m and γ = 2.39.

4.4.1. Rigid body motions

The evaluation of standard deviation of the rigid body motions is introduced in this section. For a linear system, the variance σ^2 of a given variable can be easily estimated if its transfer function $H(\omega)$ and the incident wave spectrum $S(\omega)$ are known (Faltinsen, 1993), i.e.

$$\sigma^2 = \int_0^\infty S(\omega)|H(\omega)|^2 d\omega \tag{4}$$

From Fig. 19, there are two components of surge motion, i.e. wave-frequency component and slowly varying component. The standard deviation for the former can be estimated by Eq. (4). Comparisons of the standard deviations of surge (wave-frequency component), heave and pitch from the irregular-wave tests (IRR-1 and IRR-2) with those based on Eq. (4) are shown in Fig. 25. Transfer functions used in Eq. (4) are from the white-noise test WH-1 and from WAMIT.

From Fig. 25(a), predictions based on the white-noise test and on WAMIT agree reasonably well with the experimental data for surge motion. For heave motion (see Fig. 25(b)), results based on the white-noise test are quite close to the experimental values for both cages. Results from WAMIT tend to overpredict the value for the open cage due to the WAMIT poor prediction of the heave motion (see Fig. 9(b)). From Fig. 25(c), the results based on transfer functions (i.e. using

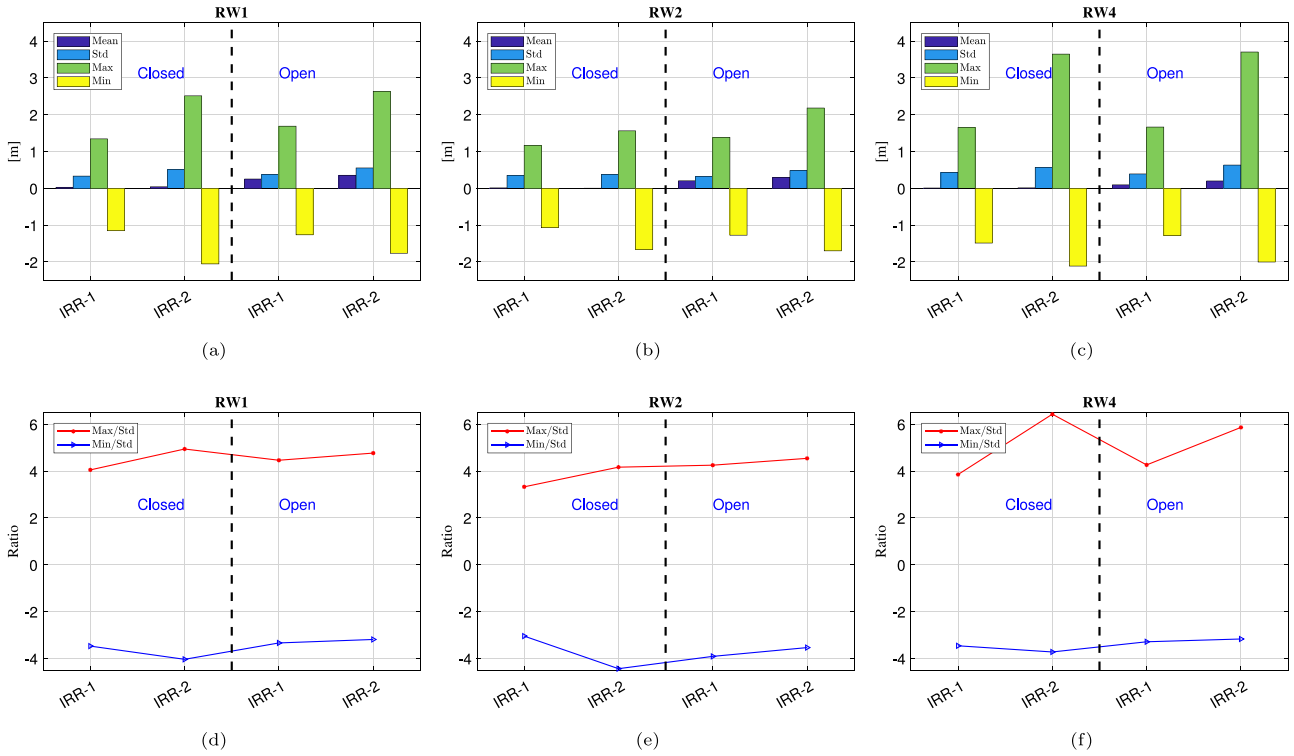

Fig. 22. Similar as in Fig. 21, but for the interior wave elevations. Left: wave probe RW1. Middle: wave probe RW2. Right: wave probe RW4.

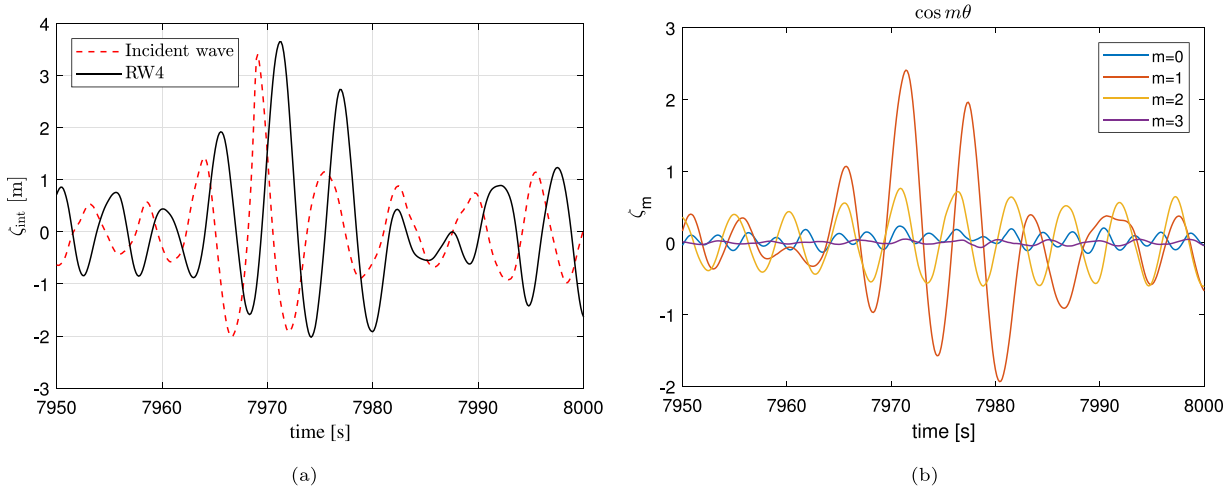

Fig. 23. (a): time history of the wave elevation from the wave probe RW4 for the closed cage in irregular wave IRR-2. Time history of the incident wave is also included for comparison. (b): time histories of different $cosm\theta$ ($m = 0 - 3$) modes that contribute to the total wave elevation from RW4.

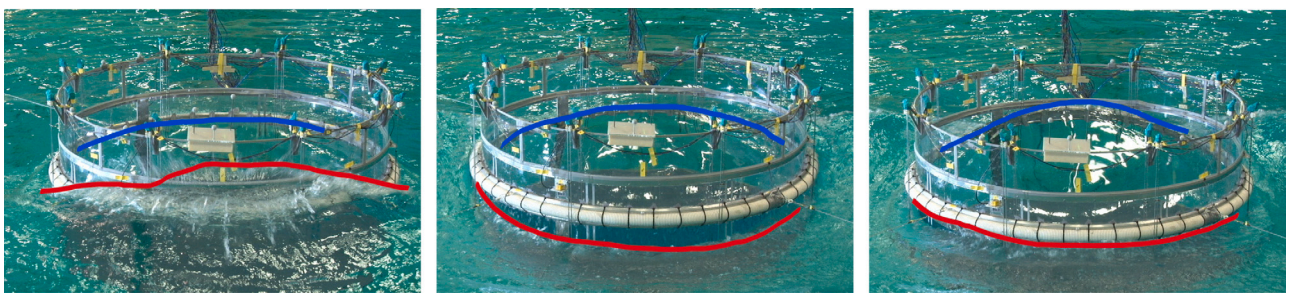

Fig. 24. Snapshots from the front camera above the water surface for the closed cage in irregular wave IRR-2. the local free-surface profiles outside and inside the cage are outlined by red and blue lines, respectively. Violent water overtopping and splash around the floating collar were observed, as shown in the left plot.

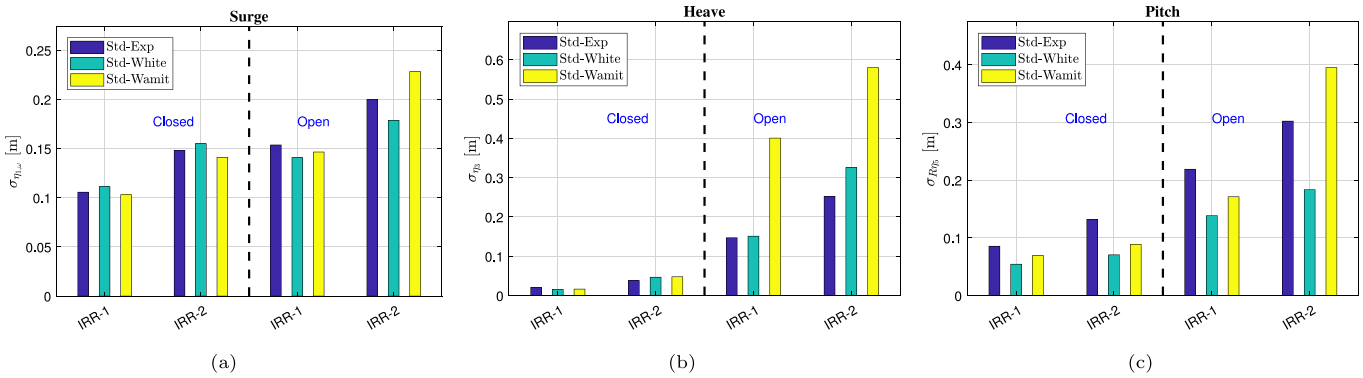

Fig. 25. Comparison of the standard deviations of surge wave-frequency component, heave and pitch between the experiments and predictions based on the white-noise test WH-1 and on WAMIT.

Eq. (4)) tend to underestimate the pitch motion for both cages. The reason is that there is an important difference-frequency component of pitch motion (see Fig. 20(b)), which is beyond the applicability of linear theory.

As shown in Fig. 19, the slowly varying component of surge motion is dominant for both cages. A brief explanation of the procedure to estimate the standard deviation of this component using the mean wave drift loads is given below. To reduce complexity, the mooring system is simplified as a linear spring with an equivalent stiffness k_s, neglecting possible hydrodynamic interaction between the incident wave and mooring lines. Moreover, the influence of the first-order response is neglected when formulating the eddy-making damping. The slow-drift surge motion $\eta_{1,s}$ of a cage can then be described by

$$\left[M + A_{11}(0)\right]\ddot{\eta}_{1,s} + B_{11}^{WD}\dot{\eta}_{1,s} + B_D\dot{\eta}_{1,s}\left|\dot{\eta}_{1,s}\right| + k_s\eta_{1,s} = F_1^{SV} \tag{5}$$

where $\ddot{\eta}_{1,s} = d^2\eta_{1,s}/dt^2$ and $\dot{\eta}_{1,s} = d\eta_{1,s}/dt$ are the slow-drift acceleration and velocity in surge, $A_{11}(0)$ is the zero frequency added mass in surge, F_1^{SV} is the slow-drift excitation force in surge. B_{11}^{WD} is the mean wave-drift damping coefficient and B_D is the quadratic damping coefficient connected with the eddy-making damping. If then the nonlinear eddy-making damping is approximated with an equivalent linear damping $B_{11}^e = 4B_D\sigma_{\dot{\eta}_{1,s}}/\sqrt{2\pi} \approx 4B_D\omega_{n,1}\sigma_{\eta_{1,s}}/\sqrt{2\pi}$ (see e.g. Faltinsen (1993) for the assumptions associated with this approximation), with $\sigma_{\eta_{1,s}}$ the standard deviation of the slowly varying component and $\omega_{n,1}$ the corresponding natural frequency, Eq. (5) can be solved in the frequency domain. The procedure does not account for the KC-dependence of B_D. According to Faltinsen (1993), the variance of the slowly varying surge motion $\eta_{1,s}$ can be written as

$$\sigma_{\eta_{1,s}}^2 = \int_0^\infty \frac{S_F(\mu)\,d\mu}{\left\{k_s - \left[M + A_{11}(0)\right]\mu^2\right\}^2 + B_{11}^2\mu^2} \tag{6}$$

Here S_F is the spectral density for the slow-drift excitation force in surge and $B_{11} = B_{11}^{WD} + B_{11}^e$. According to Pinkster (1975), the spectral density for the low-frequency part of the force, i.e. not including the mean-drift force, can be expressed in terms of the wave spectrum as

$$S_F(\mu) = 8\int_0^\infty S(\omega)S(\omega+\mu)\left[\frac{\bar{F}_1(\omega+\mu/2)}{\zeta_a^2}\right]^2 d\omega \tag{7}$$

where $S(\omega)$ is the incident wave spectrum, $\bar{F}_1/\zeta_a^2$ is the second-order transfer function of the mean wave load in surge. B_{11} is also a function of $\sigma_{\eta_{1,s}}$, so the unknown $\sigma_{\eta_{1,s}}$ is on both the left- and right-hand side of Eq. (6) and iteration is needed to obtain $\sigma_{\eta_{1,s}}$. Just a brief description is provided here, detailed explanation can be found in Shen (2018).

The quadratic damping coefficient B_D can be readily obtained from the free-decay tests, as explained in Section 2.6. The wave drift damping for the horizontal motions of a structure is connected with the structure's ability to generate waves and is a potential flow effect that neglects the interaction with flow separation. The value can be estimated using the quasi-steady approach proposed by Zhao and Faltinsen (1988) as $B_{11}^{WD} \simeq \left.\frac{\partial\bar{F}_1}{\partial U}\right|_{U=0}$, as the change of the mean-wave drift force in surge caused by the slowly-varying surge speed U. Within this quasi-steady approach, such derivative can be estimated from mean-wave drift loads in current. There are few tools available to estimate the mean drift loads for a floating body with an interior moonpool/tank, considering wave–current interaction. For simplicity, the forward-speed dependent small wavelength formula for drift force by Faltinsen (1993) is assumed be valid for all examined wavelengths

$$\bar{F}_1(\omega,U) = \left(1 + \frac{2\omega}{g}U\right)\bar{F}_1(\omega,0) \tag{8}$$

Then the wave drift damping can be estimated as

$$B_{11}^{WD} = \frac{2\omega}{g}\bar{F}_1(\omega,0) \tag{9}$$

The mean surge force in irregular waves can be estimated from its second-order transfer function and the incident-wave spectrum, as follows

$$F_{1,mean} = \int_0^\infty 2\left[\frac{\bar{F}_1(\omega)}{\zeta_a^2}\right]S(\omega)d\omega \tag{10}$$

We can then have the mean surge motion by $\bar{\eta}_1 = F_{1,mean}/k_s$, with k_s the equivalent stiffness of the system in surge (given in Section 2.3).

Fig. 26 presents a comparison of mean value of surge motion (left) and standard deviation of its slowly varying component (right). Both the experimental results and numerical predictions are provided. The mean drift loads $\bar{F}_1(\omega)$ are from WAMIT. The overall agreement is reasonable, especially for the closed cage. WAMIT provides slightly poor prediction for the open cage. One reason is that the mean drift loads were underpredicted by WAMIT in longer waves, as shown in Fig. 13. Another possible reason is that a constant drag coefficient was assumed. The actual value may be Keulegan–Carpenter (KC) number dependent due to small KC number associated (KC< 1). The contribution of the wave-drift damping is small compared with the linearized quadratic damping.

4.4.2. Interior waves

The standard deviation of the wave elevation from the different wave probes as obtained from the experiments and using Eq. (4) is documented in Fig. 27. The results from Eq. (4) are based on the transfer functions from the white-noise test WH-1 and from WAMIT. From the figure, the numerical predictions based on WH-1 agree well with the irregular-wave tests values for all the three wave probes and for both cages. Results based on WAMIT tend to underpredict the wave elevation for the closed cage. One reason is that the wave elevation induced by ovalizing deformations is not considered in WAMIT. This is especially important for the wave probe RW2 where the waves induced

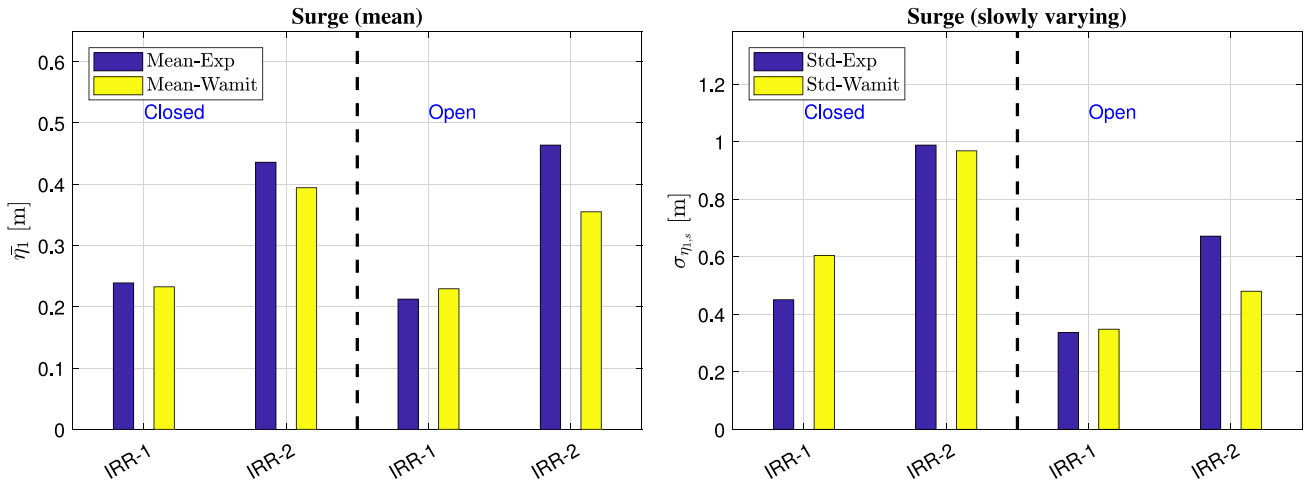

Fig. 26. Mean surge motion (left) and standard derivation of surge slowly varying component (right) from the experiments and from the predictions based on WAMIT. IRR-1: T_p = 5 s, H_s = 1.5 m and γ = 2.87. IRR-2: T_p = 6 s, H_s = 2.0 m and γ = 2.39.

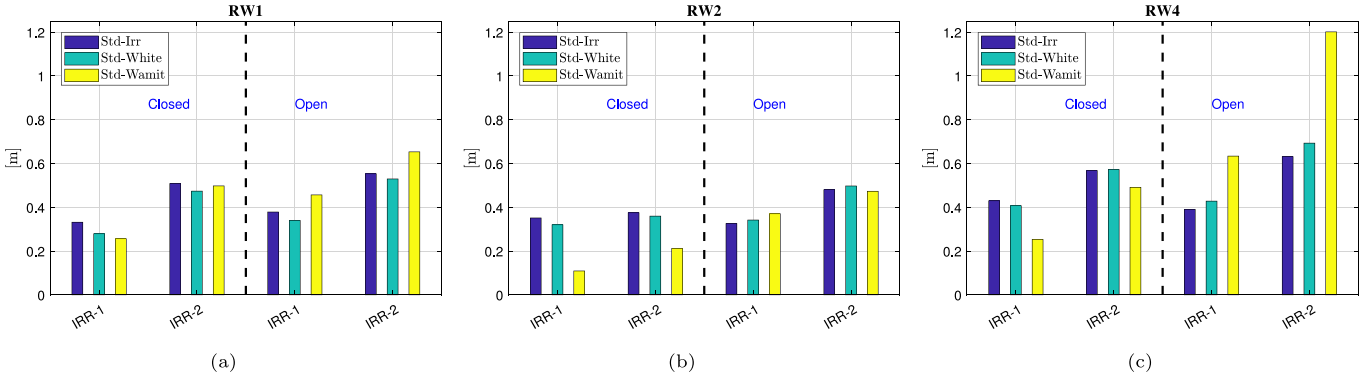

Fig. 27. Same as in Fig. 25, but for the interior wave. Left: wave probe RW1. Middle: wave probe RW2. Right: wave probe RW4.

by deformation dominate. For the semi-closed cage, the interior waves were evaluated in the body-fixed reference frame. Poor predictions of the rigid body motions, especially the heave motion, by WAMIT (see Fig. 9) would lead to unreliable predictions of the interior waves.

5. Survival conditions

There are few available investigations for the examined novel cage concepts. It would be valuable if we could provide guidance for cage design and practical operations. In this section we will try to determine the survival conditions for the two cages. Three criteria are chosen from the perspective of structural integrity and fish welfare, i.e. maximum mooring load, maximum interior wave height/minimum freeboard and maximum vertical acceleration. The mooring lines should be strong enough to withstand the environmental loads, so the maximum load in the mooring line should not yield its breaking limit. To avoid water spilling in high pitch/roll motion, the interior wave height should not exceed the freeboard. Lastly, the vertical acceleration due to cage motions and interior wave movement should be within a certain limit to avoid strong uncomfort for fish inside.

The mooring system for traditional net-based fish farms is assumed to be applicable also for novel closed/semi-closed cages. The equivalent mooring line stiffness k_s = 132.4 kN/m used in the model tests (given in Section 2.3) is larger than that of a realistic mooring system for a net-based cage given by Shen et al. (2019) for which k_s = 40 kN/m. To present a realistic set-up, the value from the latter is adopted, resulting in an increase of the natural period in surge by 76% compared with the value from the present model tests. A typical arrangement of the mooring system for a net-based fish farm is shown in Fig. 28. The force acting on the cage in surge direction is assumed to be absorbed by the front two anchor lines, neglecting the influence of small pretension in the lines and also the contribution of side mooring lines. Based on the mooring-line arrangement from Shen et al. (2019), the vertical slope of the front two anchor lines is 1/3. Then the force in one of the front anchor lines can roughly be estimated as $\sqrt{10}k_s\eta_1/6$, neglecting the influence of end catenary chain.

Assuming that local peaks of both the wave-frequency component and slow-drift component of surge motion follows the Rayleigh distribution, within a time duration t, the most probably largest value is given as

$$\eta_{1,max} = \bar{\eta}_1 + \sigma_{\eta_{1,\omega}}\sqrt{2\log(t/T_p)} + \sigma_{\eta_{1,s}}\sqrt{2\log(t/T_{n,1})} \tag{11}$$

where $\bar{\eta}_1$ is the mean surge motion, $\sigma_{\eta_{1,s}}$ and $\sigma_{\eta_{1,w}}$ are the standard deviations of the wave-frequency component and slow-drift component of the surge motion, respectively. T_p and $T_{n,1}$ are the peak wave period and the natural period in surge, respectively. Detailed approaches to estimate the different components have been introduced in Section 4.4. $\sigma_{\eta_{1,w}}$ can be estimated according to Eq. (4) based on the transfer function from the white-noise test WH-1. $\sigma_{\eta_{1,s}}$ can be obtained by Eq. (6) with mean drift loads predicted by WAMIT. The contribution of the mean surge motion $\bar{\eta}_1$ is calculated according to Eq. (10).

The most probable largest value of the anchor load $F_{\max} = k_s\eta_{1,max}$ is shown in Fig. 29 under different combinations of significant wave height H_s and peak period T_p. The considered time duration is 3 h. The examined wave conditions cover the sea states from mild exposure to heave exposure, according to the Norwegian standard shown in Table 1.

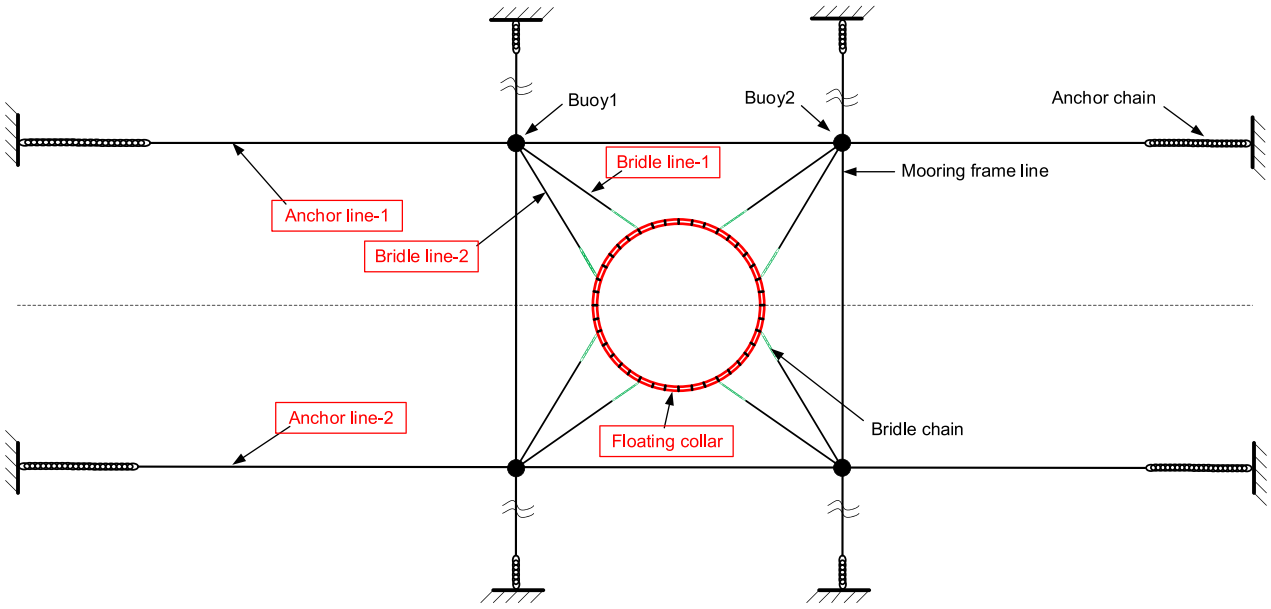

Fig. 28. Sketch of the mooring line arrangement for a traditional net-based fish farm from a top view (Shen et al., 2019). It typically comprises anchor lines, bridle lines, frame lines, supported by buoys and attached to a floating collar. The floating collar is to be replaced by a closed/semi-closed cage.

The JONSWAP wave spectrum is considered with peakedness factor $\gamma = 2.5$. From the figure, $F_{\max}$ increases with increasing significant wave height, but it is not so influenced by the peak wave period. The obtained $F_{\max}$ for the closed cage is larger than that for the open cage, due to smaller viscous damping involved. The maximum value for the closed cage is 135.4 kN while for the semi-closed one is 84.5 kN, with about 60% exceedance. The minimum breaking force for the considered anchor polysteel ropes (polysteel, 3 strand, diameter 52 mm) is about 430 kN, which is much larger than the maximum force experienced by the anchor lines. The breaking limit for the bridle lines (defined in Fig. 28) is much smaller, i.e. approximately 235 kN (polysteel, 3 strand, diameter 40 mm). In order to obtain their extreme values, a time-domain simulation considering realistic mooring lines should be performed. To reduce complexity, we assume that the bridle lines experience similar maximum load as the anchor lines, consistently with what documented by Shen et al. (2018). Then the maximum bridle load is about 57.5% of the corresponding breaking limit. This denotes that the existing mooring system for traditional fish cages could be used for the two novel cage concepts. One should note that here we just consider one cage arrangement. In reality, there may exist multiple cages that are arranged in arrays.

To prevent water spilling in large pitch/roll motion, the interior wave elevation should not exceed the freeboard of the cage. The standard deviation of the interior wave elevation at a given position $\sigma_{\zeta_{\text{int}}}$ could be predicted according to Eq. (4). Once the standard deviation is obtained, the most probable maximum wave elevation $\zeta_{int,max}$ could be given as

$$\zeta_{\text{int,max}} = \sigma_{\zeta_{\text{int}}} \sqrt{2\log(t/T_p)} \tag{12}$$

The above assumes that the local peaks of the interior wave follow the Rayleigh distribution. For a three-hour time duration, the value $\sqrt{2\log(t/T_p)}$ is close to 4 for all the considered sea states. However, the value in the model tests could reach 6 as given in Fig. 22(c) for the wave probe RW4 due to the combined influence of rigid body motions and ovalizing deformations. Here we will still use formula in Eq. (12), but the obtained value may be nonconservative.

According to Fig. 22, the largest wave elevation occurs at the back wave probe RW4 with $\theta = 202.9^{\circ}$ for both cages. Here we will examine three positions with $\theta = 0^{\circ}$, 90° and 180° at a radial position $r = 0.95R$. From the calculations, the largest interior wave elevation occurs at the backside, i.e. $\theta = 180^{\circ}$. The corresponding most probable largest elevation $\zeta_{\text{int,max}}$ is shown in Fig. 30. Unlike the anchor load, the interior wave elevation increases with increasing peak wave period T_p. The interior wave elevation for the semi-closed cage is in general slightly larger than that for the closed cage. To prevent spilling, the minimum height of the freeboard for the closed and semi-closed cage should be at least 1.05 and 1.3 m, respectively, to operate at moderate, and 2.2 m and 2.94 m, respectively, to operate at heavy exposure sea states.

Lastly, it is important to guarantee the welfare of fish inside without having too violent disturbance. One important variable could be the interior vertical acceleration. We will examine the standard deviation of vertical acceleration inside a cage. The main reason for choosing the standard deviation as an indicator is because it is commonly used for determining the operational conditions for a ship (see Faltinsen (2005)). For the closed cage, there are two contributions: rigid body motions and interior wave motion. While for the open cage, the latter is the sole contribution. Transfer function of vertical acceleration at a given interior position due to rigid body motions is estimated following Eq. (2). The part due to the interior wave is given by

$$H_{a,z}(\omega) = -\omega^2 H_{\zeta_{\text{int}}}(\omega) \tag{13}$$

where $H_{\zeta_{\text{int}}}$ is the transfer function of interior wave at a given position and could be obtained by interpolating the measurements of the eight interior wave probes RW1-8. The total standard deviation could be evaluated by following Eq. (4). Three positions were examined, i.e. front, left and aft. The largest value occurs at the aft position $\theta = 180^{\circ}$ for both cages. The standard deviations of the vertical acceleration at the backside with $r = 0.95R$ and $z = 0$ m are shown in Fig. 31. The values are made non-dimensional by the gravitational acceleration g. The maximum standard deviation for the examined wave conditions are 0.073 g and 0.075 g for the closed and semi-closed cage, respectively. Since there is no available guidance concerning the maximum vertical acceleration a fish like salmon can tolerate, we refer to operability limiting criteria for ships. There exist different criteria, for example the NORDFORSK 1987, see Faltinsen (2005). According to this criterion, the root mean square of the vertical acceleration should not exceed 0.05 g for transiting passengers. If we assume a fish like salmon resembles a human (which may not be true), then both the closed and semi-closed cage can only operate at small to moderate exposure sites.

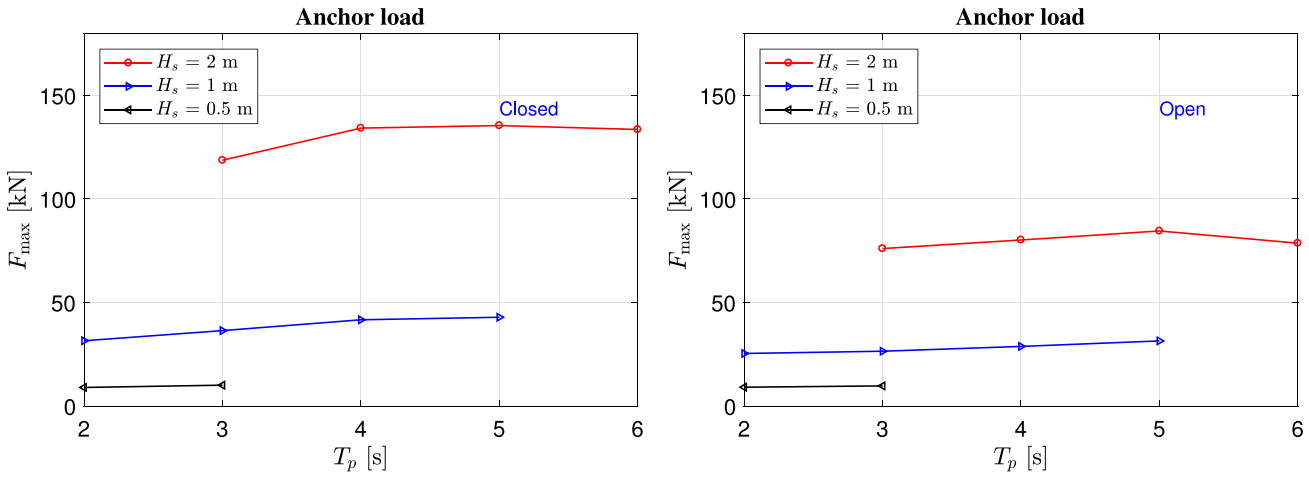

Fig. 29. Numerical predictions of the most probable maximum force in anchor lines for the closed cage (left) and semi-closed cage (right). Different combinations of significant wave height H_s and peak wave period T_p are examined.

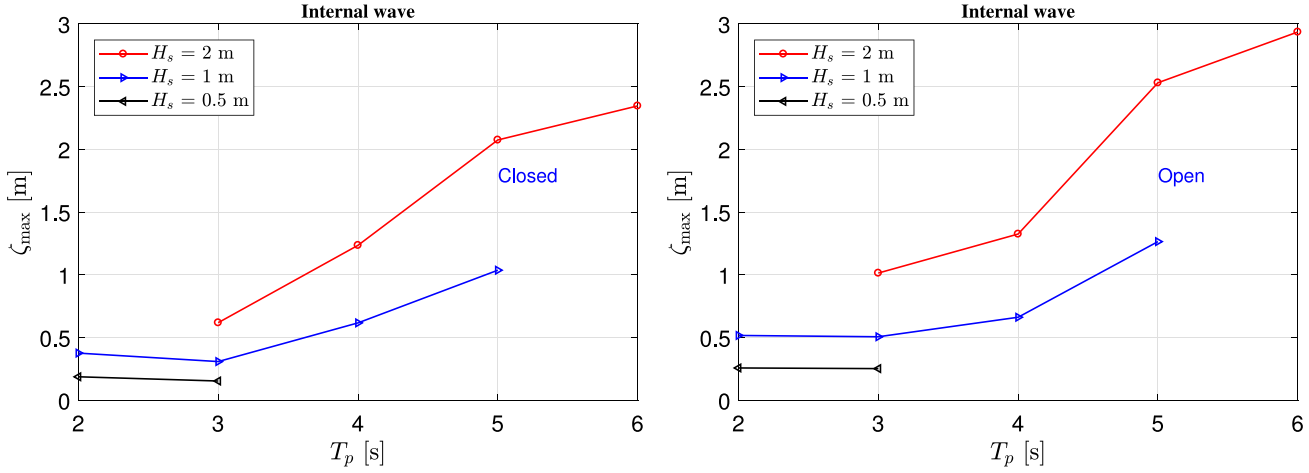

Fig. 30. Same as in Fig. 29, but for the most probable maximum interior wave elevation.

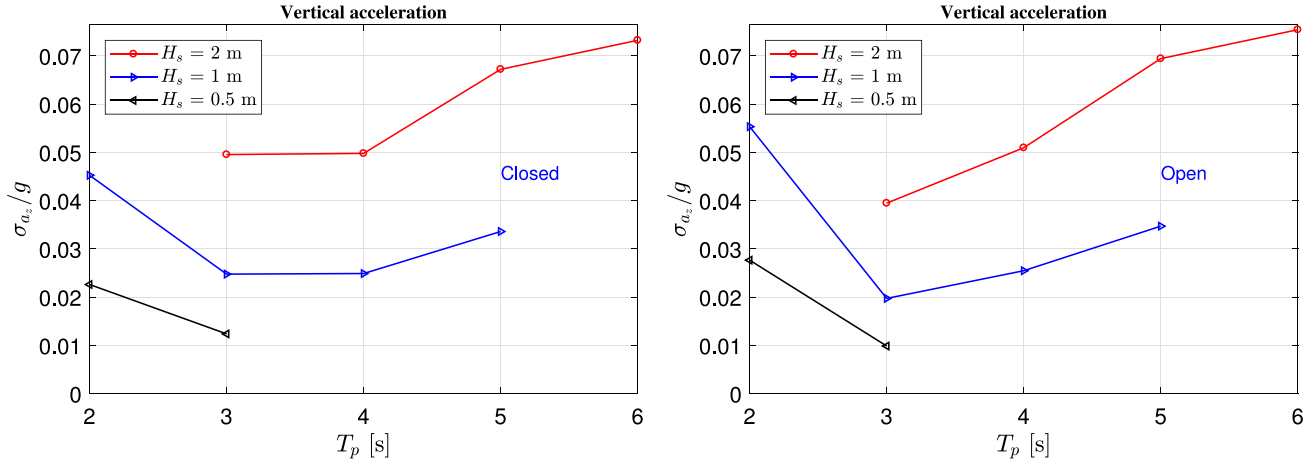

Fig. 31. Same as in Fig. 29, but for the standard deviation of interior vertical acceleration at the back side of the cage with $\theta = 180°$.

6. Conclusions

A comprehensive experimental and theoretical analysis of a novel semi-closed fish-farm cage in regular waves, white-noise waves and irregular waves has been documented, together with a detailed comparison against a closed cage with the same dimensions. Both cages consist of a vertical circular free surface-piercing cylinder with an external toroidal floater. One of the purposes was to assess the similarities and differences of the hydrodynamic behavior between the two cages. An attempt to determine the operational conditions of the two cages was also made.

Based on the theoretical and experimental studies in regular waves and white-noise waves:

- For surge motion, the semi-closed and closed cage have similar behavior for wave periods associated with local wind-generated waves. Similar trend was observed for the mean wave drift loads. The reason for the similarity is that the incident waves would nearly not feel the cage bottom for the considered waves.
- For heave motion, the closed cage experiences small response in shorter waves ($\lambda/D < 2$) and a clear resonance was observed at its natural period. For the semi-closed cage, no clear resonance was observed. A mean sinkage was detected, which is almost proportional to the square of the incident wave amplitude, indicating nonlinear behavior (at least second-order wave-body interaction effects) of the cage. A local trough also occurs at wave period associated with moonpool piston resonance.
- For pitch motion, the semi-closed cage, in general, experiences larger motion than the closed cage. A possible reason is that the former has smaller metacentric height, i.e. less stable. The maximum pitch for the semi-closed cage occurs at wave period slightly larger than the pitch natural period from the free-decay test, while it happens at the exact natural pitch period for the closed cage. A possible reason is that the natural pitch period for the semi-closed cage is altered by water-entry and water-exit phases of the floating collar.
- Both cages experience important radial ovalizing deformations, i.e. $\cos 2\theta$ mode and $\sin 2\theta$ mode. There is a small difference between the two cages for the $\cos 2\theta$ mode. For the $\sin 2\theta$ mode, the closed cage subjected to larger deformation due to stronger structural asymmetry with respect to the x-axis. Similar conclusion applies for the interior wave modes $\cos 2\theta$ and $\sin 2\theta$, which are associated with the ovalizing deformations.
- Linear potential-flow solver WAMIT, assuming a rigid body, could provide reasonable predictions of surge and pitch motions for the semi-closed cage in shorter waves ($\lambda/D < 1.5$), but not in longer waves due to increasing nonlinearities associated. Heave motion for the semi-closed cage cannot be described by linear theory. To account for the radial ovalizing deformations and associated interior waves, we need to combine a structural solver with WAMIT.

Based on the theoretical and experimental studies in irregular waves:

- For surge motion, the semi-closed and closed cage have similar behavior: (1) comparable mean surge motion; (2) dominant slowly varying motion. The standard deviation of surge motion for the closed cage is larger due to smaller viscous damping involved.
- For heave motion, similar phenomenon was observed as in regular waves: (1) the closed cage experiences much smaller heave motion compared with the semi-closed cage; (2) a clear mean sinkage is observed for the semi-closed cage.
- For pitch motion, similar phenomenon was observed as in regular waves: the semi-closed cage experiences larger pitch motion than the closed cage. For both cages, there is an important contribution outside the incident wave frequency range, which can only be excited by difference-frequency excitation.
- For interior wave elevation, both the standard deviation and maximum values are comparable between the two cages.
- The empirical approaches proposed to estimate the standard deviations for the different variables, in general, work reasonable well, except for variables associated with strong nonlinearity, for instance, pitch motion for both cages.

The survival conditions for the two cages were investigated through systematic calculations. The mooring system for a traditional net-based fish farm can be applied for the studied cages, but just for one-cage arrangement. More in-depth study is needed for cases with multiple cages arranged in an array. To prevent spilling, the minimum freeboard for the closed and semi-closed cage should be at least 1.05 and 1.3 m, respectively, to operate at moderate exposure sea states. The standard deviation of vertical acceleration due to rigid body motions and interior waves could reach 0.073 g at high exposure sea states. Whether this would exceed the tolerance limit of the fish inside needs further investigation.

CRediT authorship contribution statement

Yugao Shen: Conceptualization, Methodology, Software, Validation, Formal analysis, Investigation, Writing - original draft. **Reza Firoozkoohi:** Conceptualization, Investigation. **Marilena Greco:** Conceptualization, Writing- review & editing, Supervision. **Odd M. Faltinsen:** Conceptualization, Methodology, Writing - review & editing, Supervision.

Declaration of competing interest

The authors declare that they have no known competing financial interests or personal relationships that could have appeared to influence the work reported in this paper.

Acknowledgments

This work was supported by the Research Council of Norway through the Centers of Excellence funding scheme AMOS, project number 223254. This work has been partly funded by the Research Council of Norway, through SFI BLUES, grant number 309281.

The authors acknowledge Andrei Tsarau from Sintef Ocean for providing the experimental data. The experiments were conducted by Reza Firoozkoohi and Stefan Arenfeldt Vilsen at Sintef Ocean. The financial support for the experiments by the Research Council of Norway (grant no. 268402), the Norwegian Seafood Research Fund and the industry partners through the project Safe operation of closed aquaculture cages in waves is also appreciated.

References

Aquatraz, 2021. Semi-closed cage description. URL https://aquatraz.com/en/aquatraz-development-project.

Faltinsen, O.M., 1993. Sea Loads on Ships and Offshore Structures, Vol. 1. Cambridge University Press.

Faltinsen, O.M., 2005. Hydrodynamics of High-Speed Marine Vehicles. Cambridge University Press.

Faltinsen, O., Timokha, A., 2009. Sloshing. Cambridge University Press.

FiiZK, 2021. Lice skirt for traditional net cages. URL https://fiizk.com/en/product/lice-skirt.

Geitung, L., Oppedal, F., Stien, L.H., Dempster, T., Karlsbakk, E., Nola, V., Wright, D.W., 2019. Snorkel sea-cage technology decreases salmon louse infestation by 75% in a full-cycle commercial test. Int. J. Parasitol. 49 (11), 843–846.

Grøntvedt, R., Kristoffersen, A., 2015. Perma skirt can reduce the spread of salmon lice-field data anal-ysis. interim report permaskjørt project A5.

Hevrøy, E., Boxaspen, K., Oppedal, F., Taranger, G., Holm, J., 2003. The effect of artificial light treatment and depth on the infestation of the sea louse lepeophtheirus salmonis on atlantic salmon (salmo salar l.) culture. Aquaculture 220 (1–4), 1–14.

Huse, I., Holm, J., 1993. Vertical distribution of atlantic salmon (salmo salar) as a function of illumination. J. Fish Biol. 43, 147–156.

Iversen, A., Hermansen, Ø., Andreassen, O., Brandvik, R.K., Marthinussen, A., Nystøyl, R., 2015. Kostnadsdrivere i lakseoppdrett.

Jones, S., Beamish, R., 2011. Salmon Lice: An Integrated Approach to Understanding Parasite Abundance and Distribution. John Wiley & Sons.

Kristiansen, T., Faltinsen, O., 2008. Application of a vortex tracking method to the piston-like behaviour in a semi-entrained vertical gap. Appl. Ocean Res. 30 (1), 1–16.

Lee, C.-H., 1995. WAMIT Theory Manual. Massachusetts Institute of Technology, Department of Ocean Engineering.

Li, P., Faltinsen, O.M., 2012. Wave-induced vertical response of an elastic circular collar of a floating fish farm. In: The Intenational Conferece on HydrıDynamics. ICHD 2012.

Lien, A.M., Sunde, L.M., Bekkevoll, A., 2016. Seminar: luseskjørt og snorkelmerd-kunnskap, teknologi og metoder for best mulig utnyttelse av skjørt og snorkel for skjerming av oppdrettslaks mot lakselus, trondheim. SINTEF Fiskeri og Havbruk.

Lien, A.M., Volent, Z., Jensen, Ø., Lader, P., Sunde, L.M., 2014. Shielding skirt for prevention of salmon lice (lepeophtheirus salmonis) infestation on atlantic salmon (salmo salar l.) in cages–a scaled model experimental study on net and skirt deformation, total mooring load, and currents. Aquac. Eng. 58, 1–10.

Molin, B., 2001. On the piston and sloshing modes in moonpools. J. Fluid Mech. 430, 27.

Molin, B., Zhang, X., Huang, H., Remy, F., 2018. On natural modes in moonpools and gaps in finite depth. J. Fluid Mech. 840, 530.

Newman, J., 2018. Resonant response of a moonpool with a recess. Appl. Ocean Res. 76, 98–109.

Nilsen, A., Nielsen, K.V., Biering, E., Bergheim, A., 2017. Effective protection against sea lice during the production of atlantic salmon in floating enclosures. Aquaculture 466, 41–50.

Oppedal, F., Samsing, F., Dempster, T., Wright, D.W., Bui, S., Stien, L.H., 2017. Sea lice infestation levels decrease with deeper 'snorkel'barriers in atlantic salmon sea-cages. Pest Manag. Sci. 73 (9), 1935–1943.

Park, S., Lee, J., Lee, C.-W., 2020. Accuracy improvement of numerical simulation with the determination of drag coefficients of floating collars. Aquac. Eng. 90, 102105.

Pinkster, J.A., 1975. Low-frequency phenomena associated with vessels moored at sea. Soc. Petrol. Eng. J. 15 (06), 487–494.

Ravinthrakumar, S., Kristiansen, T., Molin, B., Ommani, B., 2020. Coupled vessel and moonpool responses in regular and irregular waves. Appl. Ocean Res. 96, 102010.

Shen, Y., 2018. Operational Limits for Floating-Collar Fish Farms in Waves and Current, Without and with Well-Boat Presence (Ph.D. thesis). Norwegian University of Science and Technology, Trondheim.

Shen, Y., Firoozkoohi, R., Greco, M., Faltinsen, O.M., 2021. Experimental investigation of a closed vertical cylinder-shaped fish cage in waves. Ocean Eng. 236, 109444.

Shen, Y., Greco, M., Faltinsen, O.M., 2019. Numerical study of a well boat operating at a fish farm in current. J. Fluids Struct. 84, 77–96.

Shen, Y., Greco, M., Faltinsen, O.M., Nygaard, I., 2018. Numerical and experimental investigations on mooring loads of a marine fish farm in waves and current. J. Fluids Struct. 79, 115–136.

StandardNorge, 2009. Marine fish farms - requirements for site survey risk, analysis, design, dimensioning, production,installation and operation. NS 9415.

Strand, I.M., Sørensen, A.J., Volent, Z., Lader, P., 2016. Experimental study of current forces and deformations on a half ellipsoidal closed flexible fish cage. J. Fluids Struct. 65, 108–120.

Xu, X., Zhang, X., Chu, B., Huang, H., 2020. On natural frequencies of three-dimensional moonpool of vessels in the fixed and free-floating conditions. Ocean Eng. 195, 106656.

Zhao, R., Faltinsen, O.M., 1988. Interaction between waves and current on a two-dimensional body in the free surface. Appl. Ocean Res. 10 (2), 87–99.